Large Impact of Approximate Exchange-Correlation Functionals on Modeling Water-gas Shift Reaction on Copper

Maliheh Shaban Tameh[†] and Chen Huang[*,‡]

[†]*Department of Scientific Computing, Florida State University, Tallahassee, Florida 32306, USA*

[‡]*Department of Scientific Computing, National High Magnetic Field Laboratory, and Materials Science and Engineering Program, Florida State University, Tallahassee, Florida 32306, USA*

E-mail: chuang3@fsu.edu

Abstract

We investigate the water-gas shift reaction (WGSR) on copper using three levels of exchange-correlation (XC) functionals of increasing complexity: Perdew-Burke-Ernzerhof (PBE) functional, Heyd-Scuseria-Ernzerhof (HSE) hybrid functional, and the exact exchange plus the random phase approximation (RPA) correlation functional. We show that DFT predictions for the kinetics of WGSR strongly depend on the choice of XC functionals. It is important to have accurate CO adsorption energy. Due to PBE's overestimation of CO's adsorption energy, it predicts small free surface and a negative (incorrect) reaction order for CO. HSE and RPA largely avoid such overestimation and predict large free surface and positive reaction orders for CO. The key finding in this work is that the prediction for WGSR mechanism also depends on the choice of XC functionals. PBE and HSE predict the carboxyl mechanism, while RPA predicts that both redox and carboxyl mechanisms are important. These results suggest that caution should be paid when using approximate XC functionals to model heterogeneous catalysis (such as WGSR investigated here) in which several mechanisms compete. In addition, we also observed one problem for RPA: It underestimates the overall WGSR energy and predicts a negative reaction order for CO_2. In addition, we examine formate's role in WGSR over copper. Both DFT and previous experiments suggest that formate does not participate much in the reaction and cannot cause a negative reaction for CO_2 for WGSR over copper.

1 Introduction

The water-gas shift reaction (WGSR) ($CO+H_2O \rightarrow CO_2+H_2$) is an important industrial process for producing hydrogen which can then be used for many applications such as ammonia production and hydrogen fuel cells.[1,2] WGSR is also an important reaction step in some heterogeneous catalysis, such as methanol synthesis and Fischer-Tropsch process. In these catalytic processes, WGSR affects H_2/CO ratio. WGSR is moderately exothermic and is slow without catalysts. It is often carried out in two stages.[1,2] In the first stage, it is carried out at high temperature (310-450 °C), which is often catalyzed by iron oxide and chromium oxide. In the second stage, it is operated at a lower temperature (200-270 °C) and is often catalyzed by copper-based catalysts.

In this work, we focus on the low-temperature WGSR whose mechanism has long been debated.[3,4] We investigate two mechanisms: the redox mechanism[5–12] and the carboxyl mechanism.[2,13–17] The main difference between them is how CO is oxidized to produce CO_2. In the redox mechanism, atomic oxygen oxidizes CO to produce CO_2. In the carboxyl mechanism, COOH is formed and then decomposes to produce CO_2.

Density functional theory (DFT)[18,19] has been widely used to gain insight into the mechanism of WGSR.[12,15,20–27] Most DFT simulations were performed using the generalized gradient approximation (GGA) exchange-correlation (XC) functionals. It is known that GGA can produce inaccurate reaction energies. For instance, GGA functionals much overestimate CO's binding energy on transition metals.[28,29] The energy barrier for water dissociation on copper can vary by as much as 0.28 eV with different GGA functionals.[30] The poor accuracy of GGA functions for describing ammonia synthesis catalyzed by iron was also reported.[31] Recently, the accuracy of XC functionals on predicting the mechanism of methanol synthesis on copper was examined.[32,33]

In this work, we investigate many aspects of the kinetics of WGSR (such as surface coverage, reaction order, dominant reaction pathway, rate-limiting step, and role of formate), in order to examine how DFT predictions depend on the choice of XC functionals. We examine three XC functionals: Perdew-Burke-Ernzerhof (PBE)[34] functional, Heyd-Scuseria-Ernzerhof (HSE)[35,36] hybrid functional, and the exact exchange (EXX) plus the random phase approximation (RPA) correlation.[37–44] They represent three different levels on Perdew's XC functional ladder.[45] We note that even if RPA functional is often expected to outperform low-level XC functionals, RPA functional has its own problem: It generally underestimates bonding energies.[44,46–48] Therefore, RPA functional still cannot reach the chemical accuracy.[49] On the other hand, RPA seems to give more accurate predictions to the relative energies. It was found that RPA much improved the adsorption energies of CO on transition metals[50] and the reaction energies for water splitting on an iron atom.[51] It is then interesting to examine the performance of RPA on modeling WGSR.

The paper is organized as follows. First, we examine the accuracy of various XC functionals for predicting the thermodynamics of WGSR. We calculate the Gibbs energy diagrams for WGSR using PBE, HSE, and RPA functionals. Based on the energy diagrams, microkinetic modeling is performed to investigate how DFT-predicted kinetics depends on XC functionals. Various aspects of WGSR are examined, such as surface coverages, reaction orders, rate-limiting steps, and dominant reaction pathways. We then discuss the role of formate in WGSR. To make the modeling more realistic, we examine how CO's converge affects the microkinetic modeling results. At last, we examine the impact of treating several adsorbates as two-dimensional (2D) ideal gases on the microkinetic modeling results.

2 Methods

2.1 DFT calculations

Most DFT calculations are performed using Vienna *Ab initio* Simulation Package (VASP)[52–56] unless specifically mentioned. We use a 3×3 Cu(211) surface with a thickness of four layers. The reason for using Cu(211) is that the reaction barriers for some key steps, such as water dissociation and CO oxidation, can be lowered by defect sites.[12,22,57,58] In addition, adsorbates often bind stronger to surface defects. The periodic images of the slab are separated by about 10 Å vacuum. PBE and HSE calculations are performed using the Fermi-Dirac smearing with a smearing temperature of 0.2 eV, a 4×4×1 Monkhorst-Pack[59] k-point mesh, and a kinetic energy cutoff of 400 eV. Gas-phase molecules are calculated by placing them in a simulation box of 10×10×10 Å. All structures are optimized using PBE functional. During the optimization, the top two Cu layers and the adsorbates are free to move. The optimized structures are then used for HSE and RPA calculations.

To reduce the cost of RPA calculations, RPA energies are obtained using the ONIOM[60] method

$$E_{\text{tot}} = E^{\text{PBE}}_{\text{total}} + (E^{\text{RPA}}_{\text{cluster}} - E^{\text{PBE}}_{\text{cluster}}), \tag{1}$$

where $E^{\text{PBE}}_{\text{total}}$ is the PBE energy of the system calculated using a kinetic energy cutoff of 400 eV and a k-point mesh of $4 \times 4 \times 1$. $E^{\text{RPA}}_{\text{cluster}}$ and $E^{\text{PBE}}_{\text{cluster}}$ are the RPA and PBE energies of the clusters, respectively, and are calculated using a lower kinetic energy cutoff (300 eV) and a smaller k-point mesh of $2 \times 2 \times 1$, in order to reduce the cost of RPA calculations. The accuracy for such smaller kinetic energy cutoff is tested in the Section IV in the Supporting Information (SI). The top two layers of Cu surface together with the adsorbates are selected as the clusters. The RPA correlation energy at infinite cutoff limit is estimated by extrapolating the results calculated using low cutoff energies.[61] In RPA calculations, the kinetic energy cutoff for expanding Kohn-Sham (KS) linear response functions is set to 2/3 of the kinetic energy cutoff (300 eV), and all unoccupied orbitals are included for constructing KS response functions. 16 frequency points are used to integrate RPA correlation energy.[62] Following Ref.[48], RPA energy is the sum of EXX energy, correction to EXX energy due to fractional occupation numbers, and RPA correlation energy. Since the clusters only contain the top two copper layers, the cost of RPA calculations are further lowered by reducing the z dimensions of simulation boxes (the surface slab is in the x-y plane), while still keeping the periodic images separated by a 10 Å vacuum.

Transition states are identified using the nudged elastic band (NEB) method,[63–65] except for the formation of formate whose transition state is located using the dimer method.[66] To reduce the computational cost of NEB, images are relaxed with the two bottom copper layers kept fixed and a small 2×2×1 k-point mesh. Such small k-point meshes are not expected to cause much error in later microkinetic modelings as discussed in Section V in SI. DFT energies of gas-phase molecules, adsorbates, and transition states are given in SI.

The Gibbs energies of CO, H_2O, CO_2, and H_2 in their gas phases are calculated as

$$G_{\mathrm{X(g)}} = E_{\mathrm{DFT,X(g)}} + \Delta G_{\mathrm{X(g)}} \tag{2}$$

where X denotes CO, H_2O, CO_2, or H_2. DFT energy ($E_{\mathrm{DFT,X(g)}}$) is calculated using VASP as described above. ΔG is the thermodynamic correction to Gibbs energy: $\Delta G = E_t + E_r + E_v - T(S_t + S_r + S_v) + k_B T$. We ignore the electronic thermodynamic contribution to Gibbs energy. $E_t = \frac{3}{2}k_B T$, $E_r = k_B T$, and $E_v = \sum_j hv_j(\frac{1}{2} + \frac{1}{\exp(hv_j/k_B T)-1})$ are the internal thermal energies due to translation, rotation, and vibration of ideal gas. $T = 473.15$ K is the WGSR temperature, k_B is the Boltzmann constant, v_j is the vibrational frequency, and h is the Planck constant. $S_t = k_B(\ln q_t + \frac{5}{2})$, $S_r = k_B(\ln q_r + 1)$, and $S_v = k_B(\ln q_v + T\frac{\partial \ln q_v}{\partial T}|_V)$ are the translational, rotational, and vibrational entropies, with q_t, q_r, and q_v being the translational, rotational, and vibrational partition functions of ideal gas. For S_v, the derivative is performed with volume V fixed. Detailed discussions on these quantities can be found in the white paper "Thermochemistry in Gaussian"[67] and can also be found in Ref.[68]. In this work, for all gas-phase molecules, ΔG is calculated using the Gaussian 09[69] program with the PBE functional and cc-pVQZ basis set.[70]

For adsorbates, we only consider the vibrational contributions to the Gibbs energies unless specifically mentioned. The Gibbs energy of X/Cu(211) is calculated as

$$G_{\mathrm{X*}} = E_{\mathrm{X*}} + E_{v,X} - TS_{v,X}. \tag{3}$$

where $E_{\mathrm{X*}}$ denotes the DFT energy of X/Cu(211) calculated using VASP, $E_{v,X}$ is internal thermal energy due to vibration, and $S_{v,X}$ is the vibrational entropy. The vibrational frequencies are obtained by diagonalizing Hessian matrices constructed using the central finite difference method. The calculations are performed using VASP with the PBE functional. The copper atoms are kept fixed to reduce the computational cost for construing Hessian matrices. For instance, for clean Cu(211) surface, the thermal correction to Gibbs energy is zero. The vibrational frequencies of all adsorbates and the transition states are given in SI.

2.2 Microkinetic modeling

Microkinetic modeling is performed at the same condition as used in Ref.[71]: 473.15 K and 1 atm total pressure with 7% CO, 8.5% CO_2, 22% H_2O, and 37% H_2 (balance inert). The reaction steps used in the modeling are listed in Table 1. For simplicity, we consider that all reaction steps take place at surface step, and we only consider one type of reaction for each reaction step and do not consider reactions to have different performance at different sites. For each reaction, we test several possible configurations at different sites and choose the one having the lowest reaction barrier. All adsorbates and transition states used for the microkinetic modelings are shown in Figs. 1 and 2. Figures are made using the VESTA program.[72] Formate is formed by reacting CO_2* with H*. We do not consider its formation through reacting OH* with CO(g), which was found unlikely to take place.[15,73]

For each reaction, its forward and backward rate constants (denoted by "+" and "−") are calculated according to the transition state theory $k^{\pm} = \frac{k_B T}{h} e^{-\Delta G_a^{\pm}/k_B T}$, where ΔG_a^{+} (ΔG_a^{-}) is the forward (backward) Gibbs reaction barrier. The coverages of CO*, H*, CO_2*, and H_2O* are calculated by assuming that they are in thermal equilibrium with their gas phases

Table 1: Elementary reactions used for the microkinetic modeling. Asterisks indicate that the intermediates are adsorbed on surface. Gas-phase molecules are marked by “(g)”. $COOH_c$ and $COOH_t$ denote the *cis* and *trans* isomers of COOH, respectively.

Redox mechanism:	
$CO(g) + * \rightarrow CO^*$	(1)
$H_2O(g) + * \rightarrow H_2O^*$	(2)
$H_2O^* + * \rightarrow H^* + OH^*$	(3)
$OH^* + * \rightarrow O^* + H^*$	(4)
$OH^* + OH^* \rightarrow H_2O^* + O^*$	(5)
$CO^* + O^* \rightarrow CO_2^* + *$	(6)
$CO_2^* + H^* \rightarrow HCOO^* + *$	(7)
$CO_2^* \rightarrow CO_2(g) + *$	(8)
$2H^* \rightarrow H_2(g) + 2*$	(9)
Carboxyl mechanism:	
$CO(g) + * \rightarrow CO^*$	(1)
$H_2O(g) + * \rightarrow H_2O^*$	(2)
$H_2O^* + * \rightarrow H^* + OH^*$	(3)
$CO^* + OH^* \rightarrow COOH_c^* + *$	(10)
$COOH_c^* \rightarrow COOH_t^*$	(11)
$COOH_t^* + * \rightarrow CO_2^* + H^*$	(12)
$COOH_t^* + OH^* \rightarrow CO_2^* + H_2O^*$	(13)
$CO_2^* + H^* \rightarrow HCOO^* + *$	(7)
$CO_2^* \rightarrow CO_2(g) + *$	(8)
$2H^* \rightarrow H_2(g) + 2*$	(9)

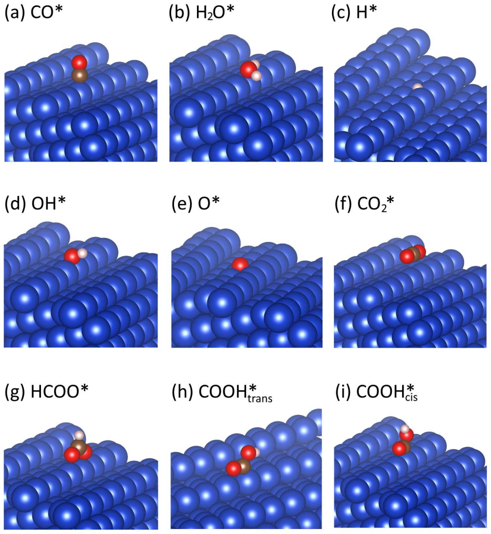

Figure 1: Adsorbates used in the microkinetic modeling. Copper, oxygen, carbon, and hydrogen atoms are blue, red, brown, and white, respectively. For easy visualization, the periodic images of the adsorbates are removed.

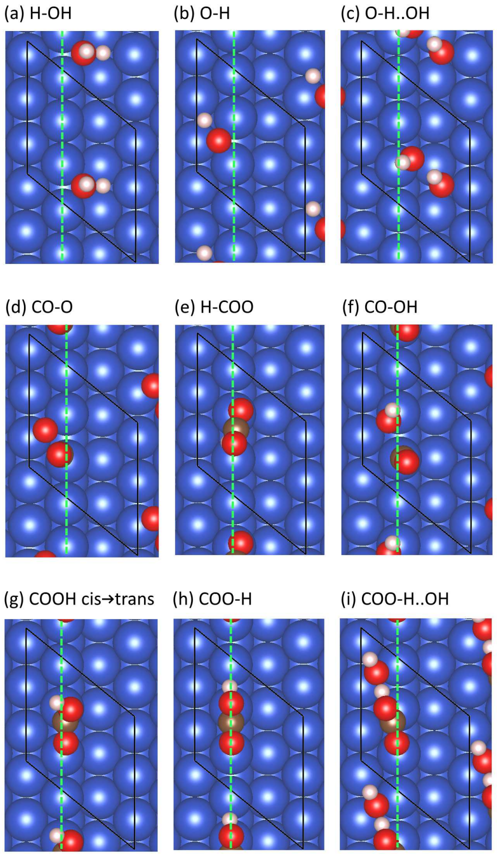

Figure 2: (a)-(i) are the top views of the transition states of reactions 3, 4, 5, 6, 7, 10, 11, 12, and 13 in Table 1, respectively. Surface steps are marked by green dashed lines. Unit cells are marked by the parallelograms.

as

$$\theta_{\mathrm{CO}} = K_1 \theta_* \tag{4}$$

$$\theta_{\mathrm{H_2O}} = K_2 \theta_* \tag{5}$$

$$\theta_{\mathrm{CO_2}} = \frac{1}{K_8} \theta_* \tag{6}$$

$$\theta_{\mathrm{H}} = \frac{1}{\sqrt{K_9}} \theta_*, \tag{7}$$

where θ_X is the coverage of adsorbate X. θ_* is the coverage of free surface. We assume that all reactions take place at the surface step, and θ_X is defined as the fractional number of X* per copper atom along the surface step. K_i is the equilibrium constant of the reaction i in Table 1. $K_1 = e^{-(G_{\mathrm{CO}*} - (G_{\mathrm{CO(g)}} + G_*))/k_B T}$, with $G_{\mathrm{CO}*}$, $G_{\mathrm{CO(g)}}$, and G_* being the Gibbs energies of CO*, CO(g), and Cu(211), respectively. Similarly, $K_2 = e^{-(G_{\mathrm{H_2O}*} - (G_{\mathrm{H_2O(g)}} + G_*))/k_B T}$, $K_8 = e^{-(G_{\mathrm{CO_2}*} - (G_{\mathrm{CO_2(g)}} + G_*))/k_B T}$, and $K_9 = e^{-(G_{\mathrm{H}*} - (\frac{1}{2} G_{\mathrm{H_2(g)}} + G_*))/k_B T}$. The rates of the reactions listed in Table 1 are calculated as

$$\begin{aligned}
r_3 &= k_3^+ \theta_* \theta_{\mathrm{H_2O}} - k_3^- \theta_{\mathrm{H}} \theta_{\mathrm{OH}} \\
r_4 &= k_4^+ \theta_* \theta_{\mathrm{OH}} - k_4^- \theta_{\mathrm{O}} \theta_{\mathrm{H}} \\
r_5 &= k_5^+ \theta_{\mathrm{OH}} \theta_{\mathrm{OH}} - k_5^- \theta_{\mathrm{O}} \theta_{\mathrm{H_2O}} \\
r_6 &= k_6^+ \theta_{\mathrm{CO}} \theta_{\mathrm{O}} - k_6^- \theta_{\mathrm{CO_2}} \theta_* \\
r_7 &= k_7^+ \theta_{\mathrm{CO_2}} \theta_{\mathrm{H}} - k_7^- \theta_{\mathrm{HCOO}} \theta_* \\
r_{10} &= k_{10}^+ \theta_{\mathrm{CO}} \theta_{\mathrm{OH}} - k_{10}^- \theta_* \theta_{\mathrm{COOH}} \\
r_{11} &= k_{11}^+ \theta_{\mathrm{COOH_c}} - k_{11}^- \theta_{\mathrm{COOH_t}} \\
r_{12} &= k_{12}^+ \theta_{\mathrm{COOH}} \theta_* - k_{12}^- \theta_{\mathrm{CO_2}} \theta_{\mathrm{H}} \\
r_{13} &= k_{13}^+ \theta_{\mathrm{COOH}} \theta_{\mathrm{OH}} - k_{13}^- \theta_{\mathrm{CO_2}} \theta_{\mathrm{H_2O}}.
\end{aligned}$$

The coverages of OH*, O*, $COOH_t$*, $COOH_c$*, and HCOO* change as

$$\begin{aligned}
\frac{d\theta_{\mathrm{OH}}}{dt} &= r_3 - r_4 - 2r_5 - r_{10} - r_{13} \\
\frac{d\theta_{\mathrm{O}}}{dt} &= r_4 + r_5 - r_6 \\
\frac{d\theta_{\mathrm{COOH_t}}}{dt} &= r_{11} - r_{12} - r_{13} \\
\frac{d\theta_{\mathrm{COOH_c}}}{dt} &= r_{10} - r_{11} \\
\frac{d\theta_{\mathrm{HCOO}}}{dt} &= r_7.
\end{aligned}$$

The free surface is calculated as

$$\theta_* = 1 - (\theta_{\mathrm{OH}} + \theta_{\mathrm{O}} + \theta_{\mathrm{COOH_c}} + \theta_{\mathrm{COOH_t}} + \theta_{\mathrm{HCOO}} + \theta_{\mathrm{H}} + \theta_{\mathrm{CO_2}} + \theta_{\mathrm{CO}} + \theta_{\mathrm{H_2O}}). \tag{8}$$

Above differential equations are integrated using the “ode15s” function in MATLAB program[74] until the steady states are reached.

3 Results and Discussions

3.1 Overall WGSR energy predicted by different XC functionals

First, we examine the accuracy of various XC functionals for predicting the overall Gibbs energy (G_{WGS}) of WGSR at 473.15 K and 1 atm total pressure with 7% CO, 8.5% CO_2, 22% H_2O, and 37% H_2. G_{WGS} is defined as

$$G_{\mathrm{WGS}} = G_{\mathrm{CO_2(g)}} + G_{\mathrm{H_2(g)}} - G_{\mathrm{CO(g)}} - G_{\mathrm{H_2O(g)}} \tag{9}$$

where $G_{\mathrm{X(g)}} = E_{\mathrm{DFT,X}} + \Delta G_{\mathrm{DFT,X}}$ is the Gibbs energy of X(g). $E_{\mathrm{DFT,X}}$ is the DFT energy of X(g) and is listed in Table S1 in SI. $\Delta G_{\mathrm{DFT,X}}$ is the thermal correction to the Gibbs energy and is calculated at the partial pressure of X(g) using the Gaussian 09 program with cc-pVQZ basis and PBE functional. $\Delta G_{\mathrm{DFT,X}}$s are listed in Table 2. The investigated XC functionals are GGA functionals (PBE, PW91,[75] RPBE,[28] and BEEF-vdW[76]), meta-GGA functionals (TPSS,[77] revTPSS,[78,79] M06-L,[80] and SCAN[81]), hybrid functionals (PBE0,[82,83] B3LPY,[84] and HSE), and RPA functional. We also calculate G_{WGS} with the coupled-cluster singles and doubles with perturbative connected triples (CCSD(T)) using the NWChem program[85] with the cc-pVTZ basis set.

Table 2: Standard enthalpy of formation ($\Delta_{\mathrm{f}} H^o_{\mathrm{X}}$), thermal correction to enthalpy ($\Delta H_{\mathrm{DFT,X}}$), and thermal correction to Gibbs energy ($\Delta G_{\mathrm{DFT,X}}$) for H_2O(g), CO(g), CO_2(g), and H_2(g). All energies are in the unit of eV.

	$\Delta_{\mathrm{f}} H^o_{\mathrm{X}}$	$\Delta H_{\mathrm{DFT,X}}$	$\Delta G_{\mathrm{DFT,X}}$
H_2O(g)	-2.506	0.651	-0.381
CO(g)	-1.145	0.218	-0.872
CO_2(g)	-4.078	0.404	-0.792
H_2(g)	0	0.347	-0.347

To calculate the experimental WGSR energy ($G^{\mathrm{exp}}_{\mathrm{WGS}}$), we need the experimental Gibbs energy of X(g), $G^{\mathrm{exp}}_{\mathrm{X(g)}}$, which is estimated as

$$G^{\mathrm{exp}}_{\mathrm{X(g)}} = \Delta_{\mathrm{f}} H^o_{\mathrm{X}} - \Delta H_{\mathrm{DFT,X}} + \Delta G_{\mathrm{DFT,X}}, \tag{10}$$

where $\Delta_{\mathrm{f}} H^o_{\mathrm{X}}$ is the standard formation enthalpy of X(g) at 293.15 K and 1 atm from NIST Webbook.[86] $\Delta H_{\mathrm{DFT,X}}$ is the thermal correction to enthalpy for X(g) at 293.15 K and 1 atm, calculated using Gaussian 09 program with cc-pVQZ basis and PBE functional. By subtracting $\Delta H_{\mathrm{DFT,X}}$, we remove the thermal component in $\Delta_{\mathrm{f}} H^o_{\mathrm{X}}$. Both $\Delta_{\mathrm{f}} H^o_{\mathrm{X}}$ and $\Delta H_{\mathrm{DFT,X}}$ are listed in Table 2. To obtain X(g)'s Gibbs energy at its partial pressure and 473.15 K, in Eq. 10 we add the thermal correction to Gibbs energy ($\Delta G_{\mathrm{DFT,X}}$) which is listed in Table 2.

The results are summarized in Fig. 3. We observe that DFT predictions for G_{WGS} much depend on the choice of XC functionals. RPA significantly underestimates G_{WGS} by 0.15 eV, while other XC functionals overestimate the WGRS energy. Compared to GGA and meta-GGA functionals, hybrid functionals less overestimate G_{WGS}. The best agreement with the experiment is from CCSD(T) with an error of 0.1 eV.

To measure how far WGSR is from the equilibrium, we calculate $\beta = \exp(-G_{\mathrm{WGR}}/k_BT)$. With $G_{\mathrm{WGS}}^{\mathrm{exp}} = -0.194$ eV, we have $\beta^{\mathrm{exp}} = 0.009$, indicating that WGSR is far from equilibrium. RPA predicts $G_{\mathrm{WGS}}^{\mathrm{RPA}} = -0.048$ eV which gives $\beta^{\mathrm{RPA}} = 0.308$, indicating that WGSR is not far from equilibrium, which is the reason for RPA to predict a negative reaction order for CO_2 as discussed in Section 3.6. This suggests that RPA functional should also be used with caution for predicting the kinetics of WGSR. Other XC functionals (GGA, meta-GGA, and hybrid) all overestimate G_{WGS} and predict that WGSR is far from equilibrium.

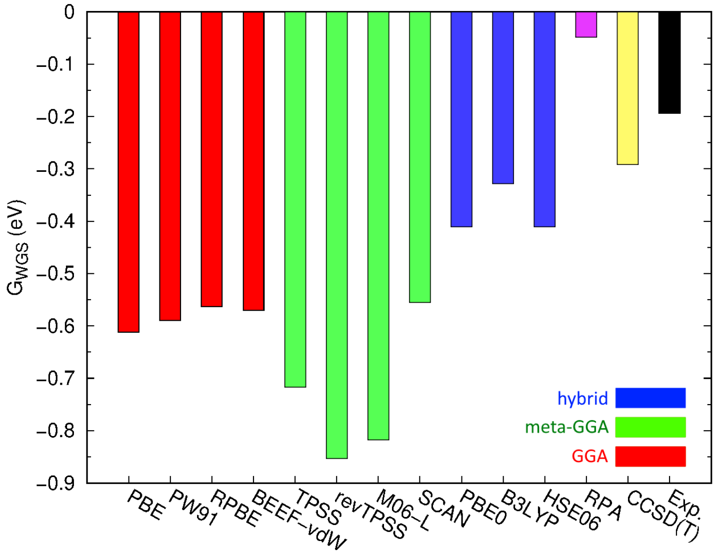

Figure 3: Overall WGSR energy calculated using different XC functionals and CCSD(T). Experimental result is denoted by "Exp."

3.2 Adsorption energies of CO, H_2O, and H_2 on Cu(211)

It is important to accurately predict the adsorption energies of CO, H_2O, and H_2 on Cu(211), since they determine the coverages of CO*, H_2O*, and H* in the microkinetic modeling.

Their adsorption energies are defined as

$$E^{\mathrm{ads}}_{\mathrm{CO}} = E_{\mathrm{CO(g)}} + E_{*} - E_{\mathrm{CO}*} \tag{11}$$

$$E^{\mathrm{ads}}_{\mathrm{H_2O}} = E_{\mathrm{H_2O(g)}} + E_{*} - E_{\mathrm{H_2O}*} \tag{12}$$

$$E^{\mathrm{ads}}_{\mathrm{H}} = \frac{1}{2}E_{\mathrm{H_2(g)}} + E_{*} - E_{\mathrm{H}*}. \tag{13}$$

In Table 3 we list the adsorption energies calculated using PBE, HSE, and RPA, which are compared to the experimental results. We find that PBE much overestimates $E^{\mathrm{ads}}_{\mathrm{CO}}$. HSE slightly overestimates $E^{\mathrm{ads}}_{\mathrm{CO}}$. RPA gives a reasonable prediction for $E^{\mathrm{ads}}_{\mathrm{CO}}$.

Table 3: Adsorption energies (in eV) for CO*, H_2O*, and H* on Cu(211) surface calculated using PBE, HSE, and RPA functionals. Experimental results are listed for comparison.

	CO*	H_2O*	H*
PBE	0.94	0.39	0.28
HSE	0.72	0.34	0.29
RPA	0.57	0.34	0.24
Exp.	0.61[87]	0.52-0.62,[88] 0.42-0.47,[90] 0.50-0.53[92]	0.16,0.34[89] 0.26[91]

Next we focus on $E^{\mathrm{ads}}_{\mathrm{H_2O}}$. We estimate the experimental $E^{\mathrm{ads}}_{\mathrm{H_2O}}$ based on the adsorption energy on Cu(110).[88,90,92] This estimation is reasonable since previous DFT studies showed that the adsorption energy of H_2O on Cu(211) is close to that on Cu(110).[93] We see that PBE, HSE, and RPA give similar predictions to $E^{\mathrm{ads}}_{\mathrm{H_2O}}$ and their predictions are smaller than the experimental results.

Let's now examine $E^{\mathrm{ads}}_{\mathrm{H}}$. To obtain experimental $E^{\mathrm{ads}}_{\mathrm{H}}$, we note that the adsorption of H_2 on copper is an activated process. The barrier for adsorption is about 0.2 eV determined via the molecular beam technique.[89] The desorption energy (at low coverage) was determined to be about 0.52 eV for Cu(110) and 0.87 eV for Cu(111) by Anger and coworker[89] and 0.71 eV for polycyrstalline copper by Kojima and coworkers.[91] $E^{\mathrm{ads}}_{\mathrm{H}}$ is set to the half of the difference between adsorption barrier and desorption energy. Table 3 shows that PBE, HSE, and RPA give similar predictions for $E_{\mathrm{H}}^{\mathrm{ads}}$ and their predictions are close to the experimental results.

In summary, PBE, HSE, and RPA give similar and good predictions to the adsorption energies of H_2O^* and H^*. For CO^*, PBE much overestimates the adsorption energy; while HSE and RPA give predictions that are close to the experiments. Later, we will show that PBE's overestimation of $E_{\mathrm{CO}}^{\mathrm{ads}}$ causes incorrect kinetics for WGSR.

3.3 Gibbs energy diagrams for the redox and carboxyl pathways

Fig. 4 gives the Gibbs energy diagrams of the redox and carboxyl mechanisms, calculated using PBE, HSE, and RPA functionals. As suggested in Ref.[94], for the redox mechanism, we consider two schemes for breaking the O-H bond in OH*: (a) directly breaking the O-H bond (reaction 4 in Table 1) and (b) the reaction between two OH* (reaction 5 in Table 1). We call scheme (b) the OH-assisted bond breaking. The direct bond breaking is denoted as TS(O-H) in Fig. 4(a). OH-assisted bond breaking is denoted by TS(O-H..OH) in Fig. 4(b). All XC functionals predict that TS(O-H..OH)+H_2(g) has a lower energy than TS(O-H)+H* (referenced to CO(g) and H_2O(g)). The reason is that OH* stabilizes O-H*, due to the interaction between the H atom in O-H* and the O atom in OH*. Similarly, for the carboxyl mechanism, we also consider two reaction schemes for breaking the O-H bond in $COOH_t^*$:[94] (a) direct bond breaking (reaction 12 in Table 1, denoted by TS(COO-H) in Fig. 4(c)) and (b) OH-assisted bond breaking (reaction 13 in Table 1, denoted by TS(COO-H..OH) in Fig. 4(d)). We also observe that, for all XC functionals, TS(COO-H..OH)+H_2(g) has a lower energy than TS(COO-H)+H* (referenced to CO(g) and H_2O(g)), due to the interaction between the H atom in COO-H* and the O atom in OH*.

The importance of having these OH-assisted reactions is that they have large impact on the highest barrier in WGSR. For both PBE and HSE, after including these OH-assisted reactions, the highest barrier changes from breaking O-H bond in Fig. 4(a) to forming CO-O bonds in Fig. 4(a) and (b). For RPA, the highest barrier changes from breaking COO-H bond in Fig. 4(c) to the step "TS(COO-H..OH)+H*" in Fig. 4(d). These changes affect the

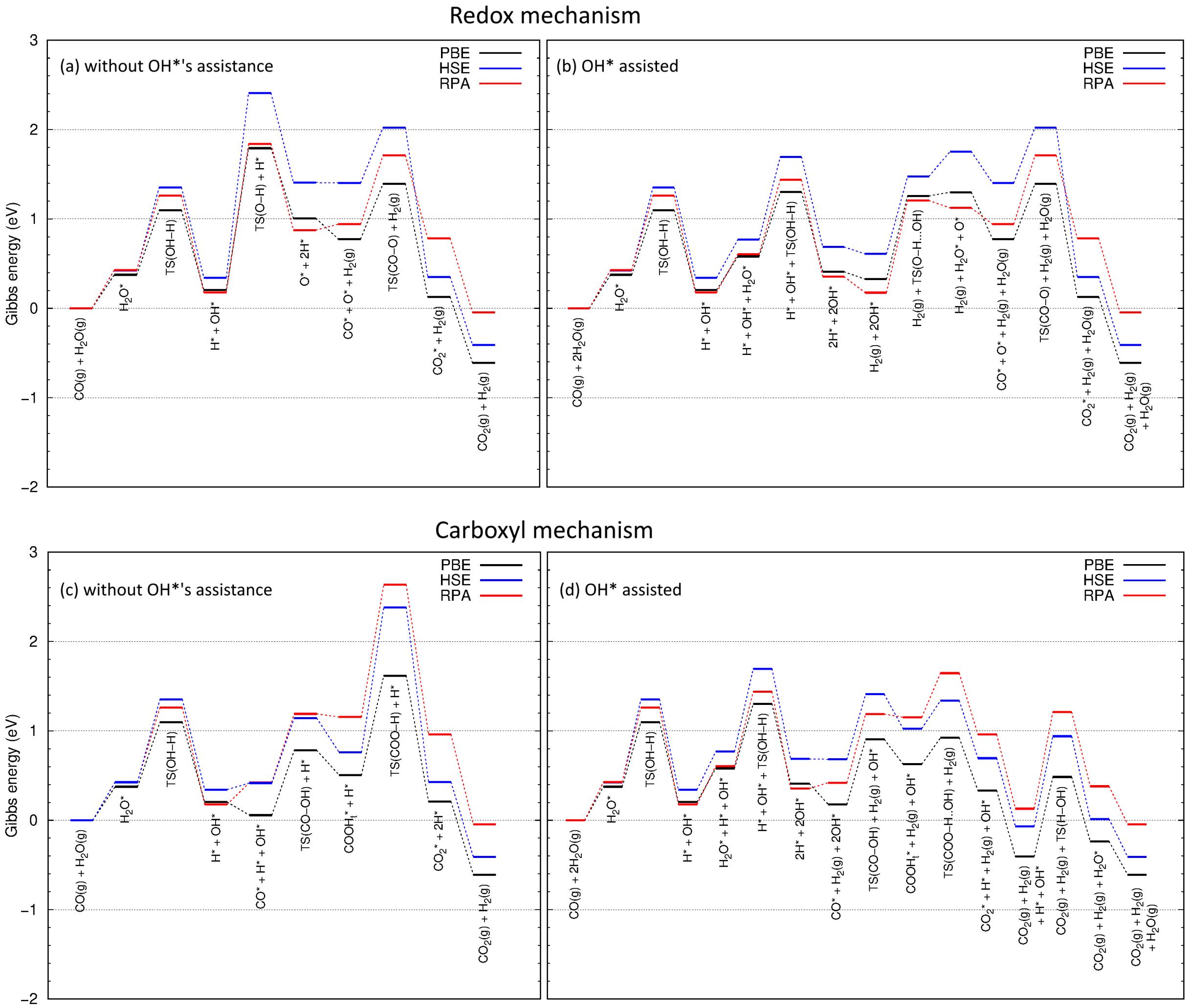

Figure 4: Gibbs energies of the redox and carboxyl pathways calculated with PBE, HSE, and RPA at 473.15 K and 1 atm total pressure with a feed composition of 7% CO, 8.5% CO_2, 22% H_2O, and 37% H_2 (balance inert). Subplots (a) and (b) are the redox mechanisms. In pathway (a), the O-H bond in OH* directly breaks. In pathway (b), the breaking of O-H bond is assisted by a nearby OH* (denoted as "O-H..OH"). Subplots (c) and (d) are the carboxyl mechanism. In pathway (c), the O-H bond in $COOH_t$* breaks directly. In pathway (d), a nearby OH* helps breaking the O-H bond in $COOH_t$* (denoted as "COO-H..OH").

rate-limiting steps. For example, as shown in Section 3.4, "TS(COO-H..OH)+H*" is one rate-limiting step for RPA functional.

3.4 Mechanism of WGSR on copper

Next, we perform microkinetic modeling based on the Gibbs energy diagrams. The turnover frequency (TOF, denoted by q) of WGSR is calculated as

$$q = \frac{r_3 + r_4 + r_{12} - r_7}{2} \tag{14}$$

where r_3, r_4, r_{12}, and r_7 are the rates of the reactions 3, 4, 12, and 7 in Table 1 for producing and consuming H*. TOF is in the unit of site^{-1}s^{-1}. "Site" refers to the sites along the surface step, since all reactions are assumed to take place on the surface step. To determine the mechanism, the contribution from the redox pathway is calculated as

$$T_{\text{redox}} = \frac{r_6}{q} \tag{15}$$

where r_6 is the rate for producing CO_2 (reaction 6 in Table 1). Reaction 6 is unique to the redox pathway, since it oxidizes CO* with O*. For the carboxyl pathway, its contribution to WGSR is calculated as

$$T_{\text{carb}} = \frac{r_{12} + r_{13}}{q} \tag{16}$$

where $r_{12} + r_{13}$ is the total rate for producing CO_2 via the dissociation of $COOH_t$* (reactions 12 and 13 in Table 1). It can be shown that $T_{\text{redox}} + T_{\text{carb}} = 1$. The rate-limiting steps are determined by calculating the degree of rate control.[95]

In Table 4, we list TOF, T_{redox}, T_{carb}, dominant mechanism, and the rate-limiting steps predicted by different XC functionals. We find that the mechanism depends on the choice of XC functionals. PBE and HSE predict that carboxyl mechanism is responsible for WGSR, as also found in previous DFT studies;[15,94] however, RPA predicts that the redox pathway is competitive with the carboxyl pathway. The prediction for rate-limiting steps also depends on the choice of XC functionals. Both PBE and HSE predicts that the main rate-limiting step is the dissociation of water, while RPA predicts that TOF is mainly limited by the steps for producing CO_2*.

Table 4: Turnover frequencies ($\mathrm{site}^{-1}\mathrm{s}^{-1}$), T_{redx}, T_{carb}, dominant mechanism, and rate-limiting steps calculated using different XC functionals. Degrees of control are listed in the parentheses.

	TOF	T_{redox}	T_{carb}	Mechanism	Rate-limiting steps
PBE	6.1×10^{-3}	0.0%	100.0%	carboxyl	$\mathrm{H_2O^* + {}^* \rightarrow H^* + OH^*}$ (95.7%) $\mathrm{COOH}_t^* + \mathrm{OH^* \rightarrow CO_2^* + H_2O^*}$ (4.2%)
HSE	4.5×10^{-3}	0.0%	100.0%	carboxyl	$\mathrm{H_2O^* + {}^* \rightarrow H^* + OH^*}$ (69.1%) $\mathrm{COOH}_t^* + \mathrm{OH^* \rightarrow CO_2^* + H_2O^*}$ (29.0%)
RPA	1.2×10^{-5}	23.1%	76.9%	carboxyl & redox	$\mathrm{COOH}_t^* + \mathrm{OH^* \rightarrow CO_2^* + H_2O^*}$ (53.2%) $\mathrm{COOH}_c^* \rightarrow \mathrm{COOH}_t^*$ (23.4%) $\mathrm{CO^* + O^* \rightarrow CO_2^* + {}^*}$ (23.1%)

Next, we show that the dominant pathways predicted by different XC functionals can be understood by analyzing the reaction steps with the highest energies on the Gibbs energy diagrams in Fig. 4. Note that for such analysis we should exclude the reaction steps that directly break the O-H and COO-H bonds, since the corresponding OH-assisted reaction steps have much lower reaction barriers. Also we should not consider the water splitting step ($\mathrm{H_2O^*+{}^* \rightarrow OH^*+H^*}$), since it is a common step for the redox and carboxyl pathways.

For PBE, the step of the highest energy in the redox pathway is to form the CO-O bond (i.e., "TS(CO-O)+H_2(g)+H_2O(g)" step) (see Fig. 4(a,b)), and the highest-energy step in the carboxyl pathway is to break the COO-H bond ("TS(COO-H...OH)+H_2(g)" step) after excluding TS(OH-H) (see Fig. 4(c,d)). The Gibbs energy for the former step is 1.39 eV which is higher than the latter step (0.92 eV), therefore PBE predicts the carboxyl pathway to be dominant. Similarly, for HSE the highest-energy steps in the redox and carboxyl pathways are the "TS(CO-O)+H_2(g)+H_2O(g)" step and the "TS(CO-OH)+H_2(g)+OH*" step (after excluding the steps having TS(OH-H)), respectively. Since the former step has a higher Gibbs energy (2.02 eV) than the latter step (1.41 eV), HSE also predicts the carboxyl pathway to be dominant. For RPA, the steps of the highest Gibbs energy in the redox and carboxyl pathways are the "TS(CO-O)+H_2(g)+H_2O(g)" step and the "TS(COO-H..OH)+H_2(g)" step, respectively. Since the Gibbs energies of the former reaction step (1.71 eV) and the latter reaction step (1.64 eV) are close, RPA predicts that the redox and carboxyl pathways are competing. This also explains the two observations in Table 4: (a) these two reaction steps are among the rate-limiting steps for RPA and (b) the carboxyl pathway is slightly faster than the redox pathway.

Another observation in Table 4 is that the water splitting step ($H_2O^*+^* \rightarrow OH^*+H^*$) is the rate-limiting step for both PBE and HSE, but not for RPA. This can be explained based on the energy diagrams (Fig. 4) as well. The reason is that the "TS(OH-H)+H*+OH*" step has the highest Gibbs energy for both PBE and HSE (Fig. 4(c,d)), but has a lower Gibbs energy than the "TS(CO-O)+H_2(g)+H_2O(g)" step for RPA (Fig. 4(a,b)).

3.5 Surface coverages predicted by different XC functionals

To assess the performance of catalysts, we need to correctly predict the amount of free surface. A small free surface indicates that the catalyst is "poisoned" during WGSR. Fig. 5(a) shows that free surface and the coverages of intermediates strongly depend on the choice of XC functionals. PBE predicts small free surface and high θ_{CO}, due to its overestimation of CO's adsorption energy (Table 3). PBE then predicts that the copper surface is poisoned by CO*. This contradicts to the previous experiments[5,24] which showed low levels of carbon on surfaces. HSE also predicts a considerable coverage for CO*, because it slightly overestimates CO's adsorption energy as seen in Table 3. RPA predicts large free surface and much lower coverages for CO*, since it slightly underestimates CO's adsorption energy.

For PBE and HSE, large free surfaces can be restored by simply correcting their predictions for CO's adsorption energy. To confirm this, we perform microkinetic modelings in which $E_{\mathrm{CO}}^{\mathrm{ads}}$ is set to the experimental value (0.61 eV). Other reaction energies are kept fixed.

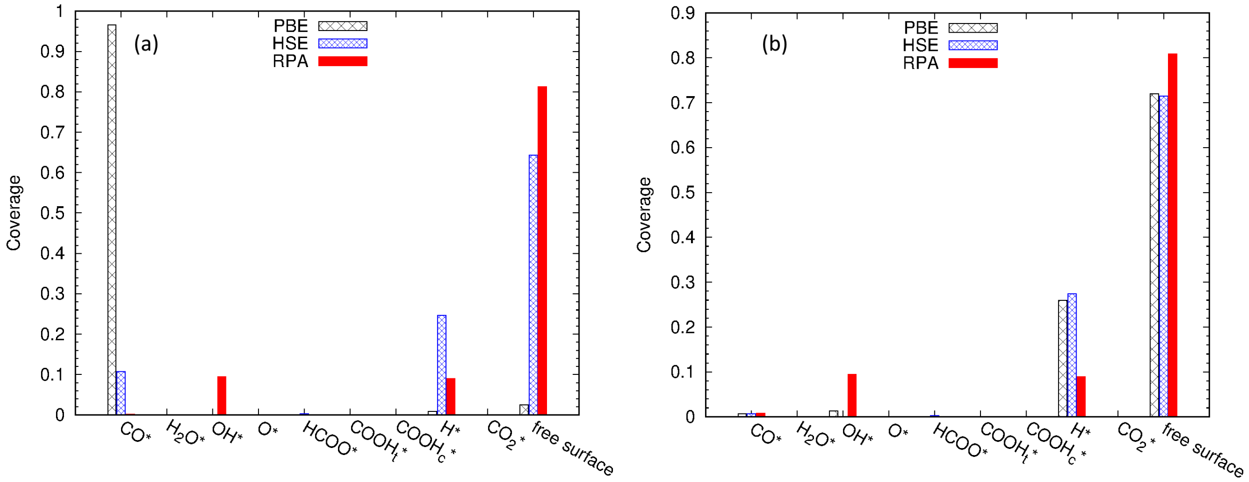

Figure 5: (a) Amount of free surface and the surface coverages of intermediates calculated using PBE, HSE, and RPA functionals. (b) Results are obtained using the experimental CO adsorption energy (0.61 eV) in microkinetic modelings.

The results are shown in Fig. 5(b). It is found that, after correcting CO's adsorption energy, both PBE and HSE predict low coverages for CO and large free surfaces. This test shows the importance of using accurate CO adsorption energy for modeling WGSR.

3.6 Apparent reaction orders

The reaction order of species i is calculated according to

$$\alpha_i = \frac{\partial \ln q}{\partial \ln P_i}$$

where P_i is the partial pressure of species i and q is TOF. Reaction orders calculated using different XC functionals are summarized in Table 5. Experimental results on Cu(111)[5] and Cu(110)[6] are listed for comparison.

3.6.1 CO reaction order

Table 5 shows that CO's reaction order depends strongly on the choice of the XC functionals. The experiments gave nearly zero reaction order for CO. PBE predicts a negative reaction

Table 5: Apparent reaction orders of CO, H_2O, CO_2, and H_2 calculated using PBE, HSE, and RPA functionals and from experiments.

	α_{CO}	$\alpha_{\mathrm{H_2O}}$	$\alpha_{\mathrm{H_2}}$	$\alpha_{\mathrm{CO_2}}$
PBE	-1.88	1.04	-0.05	0.00
HSE	0.09	1.29	-0.55	-0.01
RPA	1.44	1.81	-1.32	-0.45
Experiments:				
Cu(111)[5]	0	0.5-1		
Cu(110)[6]	0	1		

order for CO, which suggests that WGSR is hindered by increasing CO's pressure. This is again due to PBE's overestimation of CO adsorption energy. The overestimation causes copper surface to be quickly occupied by CO* as CO's pressure increases, which then inhibits WGSR and produces a negative α_{CO}. Since HSE and RPA largely avoid such overestimation, they predict positive reaction orders for CO.

To see that CO's adsorption energy has a large impact on its reaction order, we vary CO's adsorption energy ($E^{\mathrm{ads}}_{\mathrm{CO}}$) in the microkinetic modeling and keep other reaction energies fixed. The results are given in Fig. 6. It is observed that α_{CO} strongly depends on $E^{\mathrm{ads}}_{\mathrm{CO}}$. α_{CO} increases quickly as $E^{\mathrm{ads}}_{\mathrm{CO}}$ is lowered. By using the experimental $E^{\mathrm{ads}}_{\mathrm{CO}}$ (0.61 eV, marked by the dashed line), all XC functionals give a positive α_{CO}.

Table 6 shows the apparent reaction orders calculated by using the experimental $E^{\mathrm{ads}}_{\mathrm{CO}}$ (0.61 eV) and keeping other reaction energies fixed. As expected, after correcting CO's adsorption energy, all XC functionals give positive and similar α_{CO}. Compared to Table 5, we observe that $E^{\mathrm{ads}}_{\mathrm{CO}}$ also has an impact on H_2's reaction order. Both PBE and HSE give more negative $\alpha_{\mathrm{H_2}}$ after correcting CO's adsorption energy.

Table 6: Apparent reaction orders of CO, H_2O, CO_2, and H_2 calculated by using experimental CO adsorption energy ($E^{\mathrm{ads}}_{\mathrm{CO}}$=0.61 eV) in microkinetic modelings.

	α_{CO}	$\alpha_{\mathrm{H_2O}}$	$\alpha_{\mathrm{H_2}}$	$\alpha_{\mathrm{CO_2}}$
PBE	0.98	1.09	-0.69	0.00
HSE	0.79	1.72	-1.03	-0.01
RPA	1.06	1.45	-0.96	-0.09

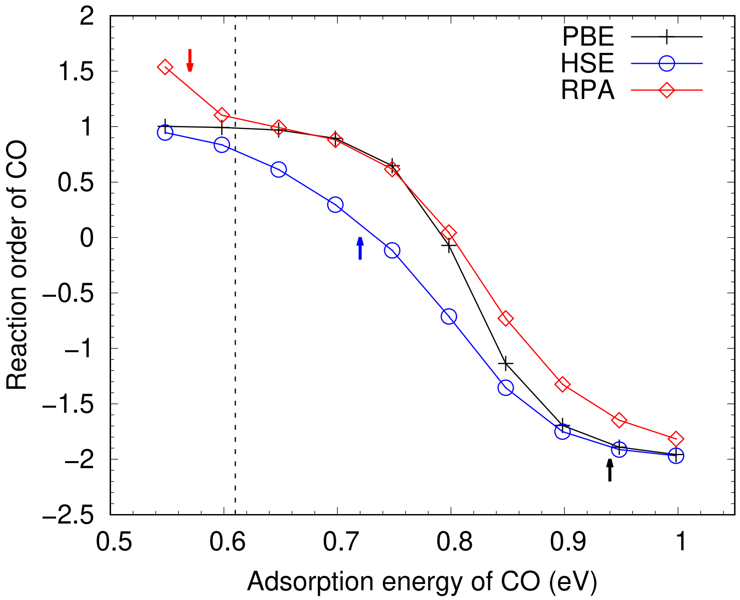

Figure 6: Dependence of CO's reaction order on its adsorption energy. PBE, HSE, and RPA adsorption energies are 0.94, 0.72, and 0.57 eV, respectively (marked by black, blue, and red arrows). Experimental adsorption energy (0.61 eV) is marked by the vertical dashed line.

3.6.2 CO_2 reaction order

In Table 5, PBE and HSE predict nearly zero reaction order for CO_2. The reason is that both PBE and HSE predict that WGSR is far from equilibrium (see Section 3.1), and then an increase of CO_2's pressure cannot effectively inhibit the WGSR. The remaining question is that why RPA predicts a negative reaction order for CO_2. The reason is that RPA underestimates G_{WGS} and predicts that WGSR is not far from equilibrium as discussed in Section 3.1. As a result, an increase in CO_2's pressure effectively inhibits WGSR. To verify our argument, for the RPA case, we re-perform microkinetic modeling in which G_{WGS} is varied by adjusting the RPA energies of CO(g), H_2O(g), H_2(g), and CO_2(g), respectively. This leads to four different microkinetic simulations. In the first simulation, we increase CO(g)'s Gibbs energy to reproduce the experimental WGSR energy ($G^{\mathrm{exp}}_{\mathrm{WGS}} = -0.194$ eV) with other energies kept fixed. This is equivalent to increase CO's adsorption energy. Similarly, in the second, third, and fourth microkinetic simulations, we adjust the RPA energies of H_2O(g), H_2(g), and CO_2(g), respectively, to reproduce $G^{\mathrm{exp}}_{\mathrm{WGS}}$. These simulations let us examine the dependence of $\alpha_{\mathrm{CO_2}}$ on G_{WGS}. The results are shown in Fig. 7. We observed that, no matter which molecule's energy is adjusted, $\alpha_{\mathrm{CO_2}}$ becomes close to zero quickly as G_{WGS} is reduced from RPA's prediction (-0.048 eV) to the experimental value (-0.194 eV). This confirms our argument that the negative $\alpha^{\mathrm{RPA}}_{\mathrm{CO_2}}$ is due to RPA's underestimation of G_{WGS}. This finding suggests that caution should also be paid when employing RPA to investigate WGSR. To identify such problem in practice, we can compare DFT's prediction for G_{WGS} against high-level methods, such as CCSD(T) as discussed in Section 3.1, to verify that whether the overall reaction energy is accurately predicted by DFT.

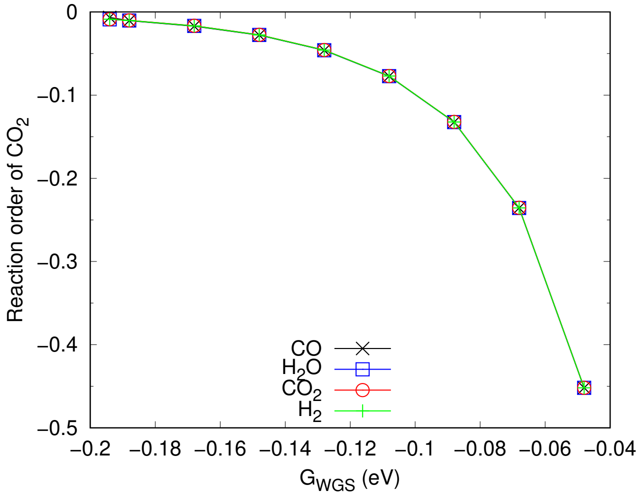

Figure 7: Dependence of $\mathrm{CO_2}$'s reaction order on the overall Gibbs energy of WGSR.

3.6.3 Formate's role in WGSR over copper

In the above section, all XC functionals predict nearly zero $\alpha_{\mathrm{CO_2}}$, when using experimental $E^{\mathrm{ads}}_{\mathrm{CO}}$. On the other hand, a negative $\alpha_{\mathrm{CO_2}}$ was observed in WGSR over industrial catalysts.[8,71] Such contradiction suggests several possibilities. (1) The active sites in industrial WGSR are metallic copper, and all XC functionals gave wrong predictions for $\alpha_{\mathrm{CO_2}}$. (2) The DFT predictions are correct; however, the reaction network used in this work misses certain key reactions that are responsible for the negative $\alpha_{\mathrm{CO_2}}$. (3) In industrial WGSR, the active sites are not metallic copper, and therefore $\alpha_{\mathrm{CO_2}}$ predicted here is irrelevant to the negative $\alpha_{\mathrm{CO_2}}$

observed in industrial WGSR.

In what follows, we focus on the possibility (1) and examine whether it is possible to have negative $\alpha_{\mathrm{CO_2}}$ for WGSR over copper. We investigate the scheme proposed by Ovesen and coworkers.[8] In that scheme, formate is responsible for the negative $\alpha_{\mathrm{CO_2}}$. Their idea is that formate is in equilibrium with CO_2(g). As we increase CO_2's pressure, formate's coverage increases, which then deactivates the copper surface and inhibits WGSR. Here, we show that this scheme is not feasible for WGSR over copper (under the assumption that the reaction network used in this work contains all the necessary reactions). We find that formate does not participate much in the WGSR over copper. Our results, however, do not rule out the possibility that formate is responsible for a negative $\alpha_{\mathrm{CO_2}}$ observed in industrial WGSR, since in these reactions the active sites may not be metallic copper.

Since formate is in quasi-thermal equilibrium with CO_2(g) and H_2(g), its coverage is determined by the following Gibbs energy difference

$$\delta G = G_{\mathrm{HCOO}*} - (G_* + G_{\mathrm{CO_2(g)}} + \frac{1}{2} G_{\mathrm{H_2(g)}}). \tag{17}$$

Then the key is to estimate experimental δG (denoted as δG^{exp}), with its calculation explained below. We consider the following three steps for forming HCOO*

1. $\mathrm{CO_2(g)} + * \rightarrow \mathrm{CO_2^*}$
2. $\mathrm{H_2(g)} + 2* \rightarrow 2\mathrm{H^*}$
3. $\mathrm{CO_2^*} + \mathrm{H^*} \rightarrow \mathrm{HCOO^*} + *.$

Based on above three steps, δG^{exp} is calculated as

$$\delta G^{\mathrm{exp}} = E_f - E_d + \Delta G_{\mathrm{thermal}}, \tag{18}$$

where E_f is the energy barrier for forming formate from $CO_2(g)$ and $H_2(g)$, that is,

$$E_f = E_{\mathrm{TS(H-COO)}} - E_* - E_{\mathrm{CO_2(g)}} - \frac{1}{2}E_{\mathrm{H_2(g)}}, \tag{19}$$

where $E_{\mathrm{TS(H-COO)}}$ is the energy of Step 3's transition state. E_d is the energy barrier for formate decomposition, that is, the backward reaction barrier of the Step 3. In Eq. 18, $\Delta G_{\mathrm{thermal}} = \Delta G_{\mathrm{HCOO*}} - \Delta G_{\mathrm{CO_2(g)}} - \frac{1}{2}\Delta G_{\mathrm{H_2(g)}}$ is included to convert $(E_f - E_d)$ to Gibbs energy, where $\Delta G_{\mathrm{HCOO*}}$, $\Delta G_{\mathrm{CO_2(g)}}$, and $\Delta G_{\mathrm{H_2(g)}}$ are the thermal corrections to the Gibbs energies for HCOO*, $CO_2(g)$, and $H_2(g)$, respectively, and are calculated using DFT with the PBE functional.

To compute δG^{exp}, we need E_f and E_d. E_d is set to the experimental activation energies for formate decomposition.[96–98,98–100] E_f is set to the experimental apparent activation barrier ($E_{\mathrm{act}}^{\mathrm{exp}}$) for the formate formation reported for different copper facets and Cu/Si_2O.[96–98,98–100] In principle, $E_{\mathrm{act}}^{\mathrm{exp}}$ is not equal to E_f, since $E_{\mathrm{act}}^{\mathrm{exp}}$ is the effective barrier for the combination of Steps 1, 2, and 3. However, it was shown that $E_f \approx E_{\mathrm{act}}^{\mathrm{exp}}$ is a good approximation since Step 3 is the rate-limiting step.[99,101] In Ref.[99], this approximation was examined for estimating E_f for formate formation on Cu(100) and the error was only 0.047 eV.

Formate's coverage is then estimated as $\theta_{\mathrm{HCOO}} = \theta_* e^{-\delta G/k_B T}$ with $T = 473.15$ K. The upper bound, $\theta_{\mathrm{HCOO}}^{\mathrm{upper}}$, is obtained by setting free surface $\theta_* = 1$. Table 7 lists DFT and experimental δG, and $\theta_{\mathrm{HCOO}}^{\mathrm{upper}}$. Both DFT and experiments give large δG, which leads to small coverages for formate and suggests that formate does not participate much in WGSR over copper. This is consistent with previous experiments in which formate was not observed after the WGS reaction on copper.[5,24] In summary, both DFT and experimental results suggest that formate cannot cause a negative $\alpha_{\mathrm{CO_2}}$ for WGSR over copper.

Table 7: Energy difference (in eV) between HCOO* and $CO_2(g)+\frac{1}{2}H_2(g)+*$ and the upper bound of formate's coverage, calculated using PBE, HSE, and RPA. Experimental results are listed for comparison.

	δG	$\theta_{\mathrm{HCOO}}^{\mathrm{upper}}$
DFT predictions:		
PBE	0.349	1.9×10^{-4}
HSE	0.222	4.3×10^{-3}
RPA	0.334	2.7×10^{-4}
Experiments:		
Cu(111)	0.72^{a}	2.1×10^{-8}
Cu(111)	0.79[98]	3.8×10^{-9}
Cu(110)	0.44[98]	2.1×10^{-5}
Cu(100)	0.29 − 0.55[99]	$8.1 \times 10^{-4} - 1.4 \times 10^{-6}$
Cu/SiO$_2$	0.73[100]	1.7×10^{-8}

[a] The apparent activation energies for the formation and decomposition of formate are taken from Ref.[96] and Ref.[97], respectively.

3.7 Effect of CO's surface coverage

Above analysis was based on the assumption that the adsorption energies do not depend on the adsorbates' converges. This assumption is good for adsorbates that have low coverages. Since PBE predicts large CO* coverage (θ_{CO}), in what follows we examine how CO's coverage affects the kinetics of WGSR.

There are three surface step sites in the simulation cell, and we can accommodate up to three CO molecules at these step sites. In this work, we do not consider the adsorption of CO on terrace, since the adsorption energies on terrace are higher. The configurations of the three coverages are shown in Fig. 8, with the adsorption energies listed in Table 8. For all XC functionals, $E_{\mathrm{CO}}^{\mathrm{ads}}$ decreases as θ_{CO} increases. To incorporate such coverage-dependent $E_{\mathrm{CO}}^{\mathrm{ads}}$ (denoted as $E_{\mathrm{CO},\theta}^{\mathrm{ads}}$) in our microkinetic modeling, for each XC functional we parameterize $E_{\mathrm{CO},\theta}^{\mathrm{ads}}$ in terms of θ_{CO} by performing piece-wise linear interpolation over three points: $(0, E_{\mathrm{CO},\theta=0}^{\mathrm{ads}})$, $(2/3, E_{\mathrm{CO},\theta=2/3}^{\mathrm{ads}})$, and $(1, E_{\mathrm{CO},\theta=1}^{\mathrm{ads}})$. For the first point, we just set $E_{\mathrm{CO},\theta=0}^{\mathrm{ads}} = E_{\mathrm{CO},\theta=1/3}^{\mathrm{ads}}$. A linear interpolation ensures that the interpolation is monotonic.

We then perform microkinetic modeling using $E_{\mathrm{CO},\theta}^{\mathrm{ads}}$. For HSE and RPA, their predictions

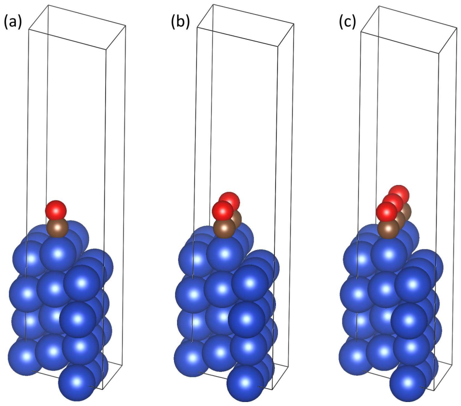

Figure 8: Three different CO coverages at surface step.

Table 8: CO adsorption energy (in eV) for different coverages on the surface step of Cu(211), calculated using PBE, HSE, and RPA functionals.

θ_{CO}	PBE	HSE	RPA
1/3	0.947	0.725	0.554
2/3	0.910	0.688	0.520
1	0.612	0.394	0.245

for adsorbates' coverages do not change much by using $E^{\text{ads}}_{\text{CO},\theta}$ (Fig. S1 in SI). For PBE, the major changes are: (a) CO's coverage decreases from 96% to 73%, (b) free surface increases from 3% to 20%, and (c) TOF increases by 46 times. The first two changes are due to the decrease of $E^{\text{ads}}_{\text{CO},\theta}$ at high CO coverage. The third change is due the increase of free surface. For all XC functionals, the dominant mechanism and rate-limiting steps (see Table S4 in SI) predicted by considering the coverage effect do not differ much from the results obtained without considering the coverage effect. The main reason is that $E^{\text{ads}}_{\text{CO},\theta}$ does not change the reaction barriers inside the redox and carboxyl pathways.

PBE's prediction for CO's reaction order is improved by using $E^{\text{ads}}_{\text{CO},\theta}$ due to the increase of free surface; however, PBE still predicts a negative reaction order (-0.23) for CO (Table S5 in SI). This shows that PBE's overestimation for CO's adsorption energy can only be alleviated, but cannot be fully resolved by considering the coverage effect. Therefore, an accurate prediction for CO's adsorption energy is essential for a reliable modeling of WGSR. On the other hand, HSE and RPA's predictions for all the reaction orders are not changed much by using $E^{\text{ads}}_{\text{CO},\theta}$ (Table S5 in SI).

3.8 Treat CO*, H_2O*, and CO_2* as 2D ideal gases

For an adsorbate whose translational barrier is smaller than k_BT, it should be treated as a 2D ideal gas, as suggested by Sellers and Campbell.[102] The adsorbate (denoted by X) retains 2/3 of its translational and rotational motion from its gas phase

$$S_{\text{X*}} = \frac{2}{3} S_{\text{X(g)}}. \tag{20}$$

In what follows, we examine this scheme by treating CO*, CO_2*, and H_2O* as 2D ideal gases, since they are molecularly bound to the surface. We find that our findings in the previous sections do not change much with this new scheme. The main reason is that the energetics in the redox and carboxyl pathways are not affected much by this new scheme, except the reaction steps that involve CO*, H_2O*, and CO_2*.

We note that this new scheme is reasonable for CO_2* which binds weakly to the surface. However, CO* and H_2O* are not really 2D ideal gases, since their translational barriers on surface are generally comparable or larger than k_BT. For instance, the barriers for CO* and H_2O* to diffuse along the surface step are 0.049 eV and 0.115 eV, respectively, which are comparable or larger than $k_BT = 0.041$ eV (with $T = 473.15$ K). Despite these observations, we still treat CO* and H_2O* as 2D ideal gases to examine the impact of this scheme on the microkinetic modeling. For other adsorbates and all the transition states, we treat them as fixed on the surface as in the previous sections, since they are either atoms or radicals that bind strongly to the surface. Large binding energies generally result large translational barriers.

Following Ref.,[103] we first need to calculate the surface concentration of CO*, CO_2*, and H_2O* (denoted as C_{CO}, C_{CO_2}, and $C_{\text{H}_2\text{O}}$, respectively). Since the entropy of a 2D ideal gas is determined by its surface concentration, the surface concentration is then related to the pressures through Eq. 20. Surface concentrations for CO*, CO_2*, and H_2O* are calculated as[103]

$$\begin{aligned} C_{\mathrm{CO}} &= e^{1/3}\left(\frac{P_{\mathrm{CO}}}{k_B T}\right)^{2/3} && (21)\\ C_{\mathrm{CO_2}} &= e^{1/3}\left(\frac{P_{\mathrm{CO_2}}}{k_B T}\right)^{2/3} && (22)\\ C_{\mathrm{H_2O}} &= e^{1/3}\left(\frac{P_{\mathrm{H_2O}}}{k_B T}\right)^{2/3}, && (23)\end{aligned}$$

respectively, where P_{CO}, $P_{\mathrm{CO_2}}$, and $P_{\mathrm{H_2O}}$ are their partial pressures. We also need to estimate the surface coverages of CO*, CO_2*, and H_2O*, because they occupy certain space along the surface step. Note that their coverages are not well defined, since they are modeled as 2D ideal gases. We first calculate their Wigner-Seitz radii as $r_{\mathrm{WS,CO*}} = (\frac{1}{4\pi C_{\mathrm{CO}}})^{1/2}$, $r_{\mathrm{WS,CO_2*}} = (\frac{1}{4\pi C_{\mathrm{CO_2}}})^{1/2}$, and $r_{\mathrm{WS,H_2O*}} = (\frac{1}{4\pi C_{\mathrm{H_2O}}})^{1/2}$. Then their coverages along the surface step are estimated as

$$\begin{aligned} \theta_{\mathrm{CO}} &= d_{\mathrm{Cu-Cu}}/r_{\mathrm{WS,CO*}} && (24)\\ \theta_{\mathrm{CO_2}} &= d_{\mathrm{Cu-Cu}}/r_{\mathrm{WS,CO_2*}} && (25)\\ \theta_{\mathrm{H_2O}} &= d_{\mathrm{Cu-Cu}}/r_{\mathrm{WS,H_2O*}} && (26)\end{aligned}$$

where $d_{\mathrm{Cu-Cu}} = 2.684$ Å is the distance between two nearest copper atoms along the surface step. The free surface is then calculated according to Eq. 8 using θ_{CO}, $\theta_{\mathrm{CO_2}}$, and $\theta_{\mathrm{H_2O}}$.

To perform microkinetic modeling, we also need the rate constants for surface reactions that involve CO*, CO_2*, and H_2O*. The rate constants are calculated following Ref.[104]. First, we calculate the Gibbs energy ($G'_{\mathrm{X*}}$) for X* (X* denotes CO*, CO_2*, or H_2O*)

$$G'_{\mathrm{X*}} = G'_{\mathrm{2D,X*}} + \Delta G_{\mu,\mathrm{X*}} \quad (27)$$

where $G'_{\mathrm{2D,X*}}$ is the Gibbs energy of X* which is treated as a 2D ideal gas

$$G'_{\mathrm{2D,X*}} = E_{\mathrm{X*}} + \frac{2}{3}\Delta G_{\mathrm{r,X(g)}} + \Delta G_{\mathrm{v,X(g)}} - k_B T \ln(q^{t'}_{\mathrm{2D,X*}}) + k_B T. \tag{28}$$

Above $E_{\mathrm{X*}}$ is the energy of X/Cu(211). $\Delta G_{\mathrm{r,X(g)}}$ is the thermal correction to Gibbs energy due to the rotation of X(g). The factor "2/3" is due to that the adsorbate keeps nearly 2/3 of its gas-phase entropy. $\Delta G_{\mathrm{v,X(g)}}$ is the thermal correction to Gibbs energy due to the vibration of X(g), and we assume that the vibrational motion of X(g) largely remains upon adsorption. $q^{t'}_{\mathrm{2D,X*}}$ is the translational partition function per area for 2D ideal gas X*

$$q^{t'}_{\mathrm{2D,X*}} = \frac{2\pi m_X k_B T}{h^2} \tag{29}$$

where m_X is the mass of X. The reason for using translational partition function *per area* is to be consistent with the use of surface concentration (C_{X}) in rate calculations, as pointed out in Ref.[104]. Note that $G'_{\mathrm{X*}}$ defined in Eq. 27 is not the Gibbs energy per molecule, because the translational term in $G'_{\mathrm{2D,X*}}$ is $-k_B T \ln(q^{t'}_{\mathrm{2D,X*}})$ rather than $-k_B T \ln(q^{t'}_{\mathrm{2D,X*}}/C_{\mathrm{X}})$.

$\Delta G_{\mu,\mathrm{X*}}$ in Eq. 27 is for preserving the overall WGSR energy. It adjusts the chemical potential of X* to match the chemical potential of X(g). The reason for such adjustment is that the chemical potentials of a 3D ideal gas and a 2D ideal gas, with the latter's entropy to be 2/3 of the former one, are not equal. On the other hand, in our microkinetic modeling the adsorption and desorption processes of X(g) are assumed to not be the rate-limiting steps, and therefore X* and X(g) should have the same chemical potentials. By including ΔG_{μ}, we restore the correct thermodynamics of the overall WGSR. The physical meaning of $G_{\mu,\mathrm{X*}}$ is that it corrects the Gibbs energy of X*, which is modeled as a 2D ideal gas but is not exactly a 2D ideal gas. $\Delta G_{\mu,\mathrm{X*}}$ is calculated as

$$\Delta G_{\mu,\mathrm{X*}} = G_{\mathrm{X(g)}} + G_{*} - G_{\mathrm{2D,X*}} \tag{30}$$

where $G_{\mathrm{2D,X*}}$ is the Gibbs energy per molecule

$$G_{\mathrm{2D,X*}} = E_{\mathrm{X*}} + \frac{2}{3}\Delta G_{\mathrm{r,X(g)}} + \Delta G_{\mathrm{v,X(g)}} - k_B T \ln\left(\frac{q^{t'}_{\mathrm{2D,X*}}}{C_{\mathrm{X}}}\right) + k_B T. \quad (31)$$

For PBE, $\Delta G_{\mu,\mathrm{CO*}}$, $\Delta G_{\mu,\mathrm{CO_2*}}$, and $\Delta G_{\mu,\mathrm{H_2O*}}$ are 0.38 eV, -0.37 eV, -0.32 eV, respectively. For HSE, they are 0.38 eV, -0.38 eV, and -0.36 eV. For RPA, they are 0.21, -0.45, -0.37 eV. By including ΔG_μ in the microkinetic modeling, the surface reactions are then fully driven by CO*, CO_2*, and H_2O* which are 2D ideal gases and have the same chemical potential as their gas phases. What Sellers-Campbell's scheme does is to change their surface coverages, which in turn affects the kinetics of WGSR.

Next we compute the rates for the surface reactions involving CO*, CO_2*, and H_2O*. Note that this work is slightly different from Ref.[104]: In this work, the reactions take place along the surface step. Let's take the surface reaction CO*+O* → CO_2*+* as an example. Following the transition state theory, the rate of the forward reaction is $r_f = \frac{k_B T}{h}\frac{q_\ddagger}{(Wq'_{\mathrm{2D,CO*}})q_{\mathrm{O*}}}(WC_{\mathrm{CO}})\theta_{\mathrm{O}}$, where W is the width of the surface step. Since Ws in the denominator and numerator are canceled out, we do not need to know the exact value for W. WC_{CO} gives the linear density of CO* along the surface step. $q'_{\mathrm{2D,CO*}}$ is CO*'s partition function and is the product of translational ($q^{t'}_{2D}$), vibrational (q^v), rotational (q^r), and electronic (q^e) contributions: $q'_{\mathrm{2D,CO*}} = q^{t'}_{2D} q^v q^r q^e$. $q^{t'}_{2D}$ is defined in eq. 29. $Wq'_{\mathrm{2D,CO*}}$ gives the partition function per unit length along the surface step. In practice, we calculate r_f by rewriting it in terms of Gibbs energies: $r_f = \frac{k_B T}{h} C_{\mathrm{CO}}\theta_{\mathrm{O}} e^{-(G_\ddagger - G'_{\mathrm{CO*}} - G_{\mathrm{O*}})/k_B T}$. $G_\ddagger$ is the Gibbs energy of the transition state which is assumed to be fixed on the surface, and only the vibrational contribution to $G_\ddagger$ is considered. Similarly, the rate of the backward reaction is calculated as $r_b = \frac{k_B T}{h} C_{\mathrm{CO_2}}\theta_* e^{-(G_\ddagger - G'_{\mathrm{CO_2*}} - G_*)/k_B T}$.

Following above procedures, we perform microkinetic modeling. Adsorbate coverages (denoted by "2D gas") are summarized in Fig. 9. For comparison, we also show the coverages calculated by assuming that all adsorbates are fixed on the surface and the results are denoted by “Fixed”. We note that the coverages of CO*, CO_2*, and H_2O* are independent of XC functionals, since they are fully determined by their pressures. As a result, PBE now predicts large free surface and small CO coverage. PBE’s prediction for CO’s reaction order is also improved as shown in Table 9: A positive CO reaction order is predicted by PBE.

Table 9: Similar to Table 5. Apparent reaction orders are calculated by treating CO*, CO_2*, and H_2O* as 2D ideal gases.

	α_{CO}	$\alpha_{\mathrm{H_2O}}$	$\alpha_{\mathrm{H_2}}$	$\alpha_{\mathrm{CO_2}}$
PBE	0.87	0.99	-0.45	0.00
HSE	0.04	0.91	-0.10	-0.02
RPA	1.24	1.77	-1.05	-0.20

Fig. 9 also shows that formate’s coverages are still nearly zero with treating CO*, CO_2*, and H_2O* as 2D ideal gases. The reason is that the relative energy between $CO_2(g)+\frac{1}{2}H_2(g)+*$ and HCOO* does not change with this new scheme. Therefore our previous conclusion that formate is unlikely to be the cause for the negative CO_2 reaction order for WGSR on copper still holds.

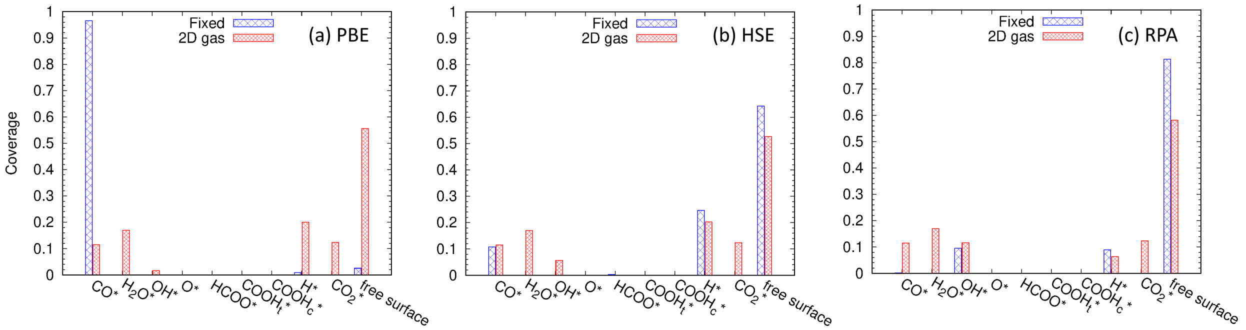

Figure 9: Adsorbate coverages calculated using different XC functionals. “Fixed” denotes that the adsorbates are fixed on surface. “2D gas” denotes that CO*, CO_2* and H_2O* are modeled as 2D ideal gases.

In Table 10, we list the turnover frequencies, dominant mechanism, and rate-limiting steps obtained by treating CO*, CO_2*, and H_2O* as 2D ideal gases. The predictions for the dominant mechanism are similar to the previous case (see Table 4): PBE and HSE still predict the carboxyl pathway to be dominant, while RPA predicts that both redox and carboxyl pathways are important. This is not surprising, since the new treatment of

CO*, CO_2*, and H_2O* does not affect the Gibbs energies of the transition states inside the carboxyl and redox pathways. Table 10 also shows that PBE's TOF increases significantly compared to the previous case (Table 4). The reason is that Sellers-Campbell's scheme gives large free surface (see Fig. 9(a)).

Table 10: Similar to Table 4. The turnover frequencies (site^{-1}s^{-1}), dominant mechanism, and rate-limiting steps are calculated by treating CO*, CO_2*, and H_2O* as 2D ideal gases. The degrees of control are listed in the parentheses.

	TOF	T_{redox}	T_{carb}	Mechanism	Rate-limiting steps
PBE	6.9×10^{-1}	0.4%	99.6%	carboxyl	CO* + OH* → $COOH_c$* + * (87.2%) H_2O* + * → H* + OH* (11.8%)
HSE	1.1×10^{-2}	0.3%	99.7%	carboxyl	H_2O* + * → H* + OH* (94.3%) CO* + OH* → $COOH_c$* + * (5.6%)
RPA	2.6×10^{-5}	19.2%	80.8%	carboxyl & redox	$COOH_t$* +OH* → CO_2* + H_2O* (40.1%) $COOH_t$* → $COOH_c$* (22.0%) CO* + O* → CO_2* + * (19.2%) CO* + OH* → $COOH_c$* + * (17.6%)

3.9 Van der Waals effect

In the previous sections, PBE predicts that carboxyl pathway is dominate, while RPA predicts that both carboxyl and redox pathways are important. To investigate whether such discrepancy is due to the lack of van der Waals (vdW) interaction in PBE functional, we performed additional DFT-D3 calculations.[105] The vdW interactions are parameterized based on the PBE functional. Structures of adsorbates and transition states are re-optimized using the DFT-D3 functional, and the vibrational frequencies of the adsorbates and transition states are then calculated using the DFT-D3 functional, based on which thermal corrections to Gibbs energies are calculated. The results are listed in Table S.8 in SI. Microkinetic modeling is then performed based on DFT-D3 results. Overall, DFT-D3 results are similar to PBE results. DFT-D3 predicts T_{carb}=100%, a TOF of 0.0084 site^{-1}s^{-1}, and the rate-limiting step to be H_2O* + * → H* + OH* (with a degree of control of 99.6%). The similarity between

DFT-D3 and PBE results suggests that the difference between PBE and RPA predictions is not due to vdW interaction but is mainly due to their different descriptions of short-range chemical bonding between atoms.

4 Conclusions

Nowadays, DFT is widely used for modeling catalysis. In this work, we performed microkinetic modeling of WGSR on copper using three levels of XC functionals (PBE, HSE, and RPA functionals) to investigate how the choice of XC functionals affects DFT's predictions. We found that the predicted kinetics of WGSR strongly depends on the choice of the XC functionals. It is important to accurately predict CO adsorption energy which has a large impact on the amount of free surface and CO coverage, as well as on CO and H_2's reaction orders. For instance, due to PBE's overestimation of CO's adsorption energy, it predicts a high level of carbon (which contradicts to experiments) and a negative CO reaction order. These issues can be fixed by simply correcting CO adsorption energy. The importance of using accurate CO adsorption energy was also pointed out by Zhao and coworkers recently.[106] By using HSE values, CO's binding energy was improved which led to lower CO coverage and a positive CO reaction order. In this work, we also investigated whether formate can cause a negative CO_2 reaction order for WGSR on copper. Our DFT results and previous experiment results all suggest that formate has a low coverage and does not participate much in the WGSR on copper. Therefore, CO_2's negative reaction order, observed in WGSR over industrial catalysts, should be due to other reasons.

An important observation in this work is that DFT predictions for the mechanism of WGSR depend on the choice of XC functionals. PBE and HSE predict carboxyl mechanism to be dominant, while RPA predicts both redox and carboxyl mechanisms are important. Such observation does not change by considering coverage-dependent CO adsorption energy, treating CO^*, CO_2^*, and H_2O^* as 2D ideal gases, or considering vdW effect. Our findings suggest that caution should be taken when employing approximate XC functionals to investigate catalytic processes, such as WGSR, in which several competing reaction pathways exist. Note that the goal of this work is not to show that RPA functional is more accurate than other functionals on modeling WGSR. Actually, RPA functional has its own problem: It underestimates the overall WGSR energy, which has a large impact on its prediction for CO_2's reaction order. This work suggests that future development of accurate and computationally efficient XC functionals is required to achieve reliable modeling of WGSR.

Supporting Information Available

The Supporting Information contains (a) DFT energies and vibrational frequencies of gas-phase molecules, adsorbates, and transition states, (b) microkinetic modeling results based on $E^{\mathrm{ads}}_{\mathrm{CO},\theta}$, (c) and the convergence tests for RPA calculations. This material is available free of charge via the Internet at http://pubs.acs.org.

Acknowledgement

This work is supported by the Florida State University (start-up fund) and National Science Foundation under CHE-1752769.

References

(1) Newsome, D. S. The Water-Gas Shift Reaction. *Catalysis Reviews* **1980**, *21*, 275–318.

(2) Rhodes, C.; Hutchings, G.; Ward, A. Water-gas shift reaction: finding the mechanistic boundary. *Catal. Today* **1995**, *23*, 43–58.

(3) Ratnasamy, C.; Wagner, J. P. Water Gas Shift Catalysis. *Catalysis Reviews* **2009**, *51*, 325–440.

(4) Smith, B.; Loganathan, M.; Shantha, M. S. A Review of the Water Gas Shift Reaction Kinetics. *Int. J. Chem. React. Eng.* **2010**, *8*, 1.

(5) Campbell, C.; Daube, K. A surface science investigation of the water-gas shift reaction on Cu(111). *J. Catal.* **1987**, *104*, 109–119.

(6) Nakamura, J.; Campbell, J. M.; Campbell, C. T. Kinetics and mechanism of the water-gas shift reaction catalyzed by the clean and Cs-promoted Cu(110) surface: a comparison with Cu(111). *J. Chem. Soc., Faraday Trans.* **1990**, *86*, 2725–2734.

(7) Ovesen, C.; Stoltze, P.; Nørskov, J.; Campbell, C. A kinetic model of the water gas shift reaction. *J. Catal.* **1992**, *134*, 445–468.

(8) Ovesen, C.; Clausen, B.; Hammershøi, B.; Steffensen, G.; Askgaard, T.; Chorkendorff, I.; Nørskov, J.; Rasmussen, P.; Stoltze, P.; Taylor, P. A Microkinetic Analysis of the Water–Gas Shift Reaction under Industrial Conditions. *Journal of Catalysis* **1996**, *158*, 170–180.

(9) Yoshihara, J.; Campbell, C. T. Methanol Synthesis and Reverse Water–Gas Shift Kinetics over Cu(110) Model Catalysts: Structural Sensitivity. *J. Catal.* **1996**, *161*, 776–782.

(10) Waugh, K. Prediction of global reaction kinetics by solution of the Arrhenius parameterised component elementary reactions: microkinetic analysis. *Catal. Today* **1999**, *53*, 161–176.

(11) Schumacher, N.; Boisen, A.; Dahl, S.; Gokhale, A. A.; Kandoi, S.; Grabow, L. C.; Dumesic, J. A.; Mavrikakis, M.; Chorkendorff, I. Trends in low-temperature water–gas shift reactivity on transition metals. *J. Catal.* **2005**, *229*, 265–275.

(12) Wang, G.-C.; Nakamura, J. Structure sensitivity for forward and reverse water-gas

shift reactions on copper surfaces: a DFT study. *J. Phys. Chem. Lett.* **2010**, *1*, 3053–3057.

(13) Clarke, D.; Bell, A. An Infrared Study of Methanol Synthesis from CO2 on Clean and Potassium-Promoted Cu/SiO2. *J. Catal.* **1995**, *154*, 314–328.

(14) Callaghan, C.; Fishtik, I.; Datta, R.; Carpenter, M.; Chmielewski, M.; Lugo, A. An improved microkinetic model for the water gas shift reaction on copper. *Surface Science* **2003**, *541*, 21–30.

(15) Gokhale, A.; Dumesic, J.; Mavrikakis, M. On the mechanism of low-temperature water gas shift reaction on copper. *J. Am. Chem. Soc.* **2008**, *130*, 1402–1414.

(16) Madon, R.; Braden, D.; Kandoi, S.; Nagel, P.; Mavrikakis, M.; Dumesic, J. Microkinetic analysis and mechanism of the water gas shift reaction over copper catalysts. *J. Catal.* **2011**, *281*, 1–11.

(17) Yang, Y.; Mims, C.; Mei, D.; Peden, C.; Campbell, C. Mechanistic studies of methanol synthesis over Cu from CO/CO2/H2/H2O mixtures: The source of C in methanol and the role of water. *J. Catal.* **2013**, *298*, 10–17.

(18) Hohenberg, P.; Kohn, W. Inhomogeneous Electron Gas. *Phys. Rev.* **1964**, *136*, B864–B871.

(19) Kohn, W.; Sham, L. J. Self-consistent equations including exchange and correlation effects. *Phys. Rev.* **1965**, *140*, A1133.

(20) Jakdetchai, O.; Nakajima, T. Mechanism of the water–gas shift reaction over Cu(110), Cu(111) and Cu(100) surfaces: an AM1-d study. *J. Mol. Struct.: THEOCHEM* **2002**, *619*, 51–58.

(21) Greeley, J.; Nørskov, J. K.; Mavrikakis, M. Electronic structure and catalysis on metal surfaces. *Annual Review of Physical Chemistry* **2002**, *53*, 319–348.

(22) Wang, G.; Jiang, L.; Cai, Z.; Pan, Y.; Zhao, X.; Huang, W.; Xie, K.; Li, Y.; Sun, Y.; Zhong, B. Surface Structure Sensitivity of the Water-Gas Shift Reaction on Cu(hkl) Surfaces: A Theoretical Study. *J. Phys. Chem. B* **2003**, *107*, 557–562.

(23) Liu, P.; Rodriguez, J. Water-gas-shift reaction on metal nanoparticles and surfaces. *J. Chem. Phys.* **2007**, *126*, 164705.

(24) Rodriguez, J.; Liu, P.; Hrbek, J.; Evans, J.; Pérez, M. Water Gas Shift Reaction on Cu and Au Nanoparticles Supported on CeO2(111) and ZnO(000): Intrinsic Activity and Importance of Support Interactions. *Angew. Chem. Int. Ed.* **2007**, *46*, 1329–1332.

(25) Grabow, L. C.; Gokhale, A. A.; Evans, S. T.; Dumesic, J. A.; Mavrikakis, M. Mechanism of the Water Gas Shift Reaction on Pt: First Principles, Experiments, and Microkinetic Modeling. *J. Phys. Chem. C* **2008**, *112*, 4608–4617.

(26) Tang, Q.-L.; Chen, Z.-X.; He, X. A theoretical study of the water gas shift reaction mechanism on Cu(111) model system. *Surf. Sci.* **2009**, *603*, 2138–2144.

(27) Huang, S.-C.; Lin, C.-H.; Wang, J.-H. Trends of water gas shift reaction on close-packed transition metal surfaces. *J. Phys. Chem. C* **2010**, *114*, 9826–9834.

(28) Hammer, B.; Hansen, L. B.; Nørskov, J. K. Improved adsorption energetics within density-functional theory using revised Perdew-Burke-Ernzerhof functionals. *Phys. Rev. B* **1999**, *59*, 7413–7421.

(29) Feibelman, P.; Hammer, B.; Nørskov, J.; Wagner, F.; Scheffler, M.; Stumpf, R.; Watwe, R.; Dumesic, J. The CO/Pt(111) puzzle. *J. Phys. Chem. B* **2001**, *105*, 4018–4025.

(30) Fajín, J. L. C.; Illas, F.; Gomes, J. R. B. Effect of the exchange-correlation potential and of surface relaxation on the description of the H2O dissociation on Cu(111). *The Journal of Chemical Physics* **2009**, *130*, 224702.

(31) Kepp, K. P. Accuracy of theoretical catalysis from a model of iron-catalyzed ammonia synthesis. *Communications Chemistry* **2018**, *1*, 63.

(32) Studt, F.; Abild-Pedersen, F.; Varley, J.; Nørskov, J. CO and CO_2 Hydrogenation to Methanol Calculated Using the BEEF-vdW Functional. *Catal. lett.* **2013**, *143*, 71–73.

(33) Tameh, M. S.; Dearden, A. K.; Huang, C. Accuracy of Density Functional Theory for Predicting Kinetics of Methanol Synthesis from CO and CO2 Hydrogenation on Copper. *The Journal of Physical Chemistry C* **2018**, *122*, 17942–17953.

(34) Perdew, J.; Burke, K.; Ernzerhof, M. Generalized gradient approximation made simple. *Phys. Rev. Lett.* **1996**, *77*, 3865.

(35) Heyd, J.; Scuseria, G.; Ernzerhof, M. Hybrid functionals based on a screened Coulomb potential. *J. Chem. Phys.* **2003**, *118*, 8207–8215.

(36) Krukau, A. V.; Vydrov, O. A.; Izmaylov, A. F.; Scuseria, G. E. Influence of the exchange screening parameter on the performance of screened hybrid functionals. *J. Chem. Phys* **2006**, *125*, 224106.

(37) Bohm, D.; Pines, D. A Collective Description of Electron Interactions. I. Magnetic Interactions. *Phys. Rev.* **1951**, *82*, 625–634.

(38) McLachlan, A.; Ball, M. Time-Dependent Hartree-Fock Theory for Molecules. *Rev. Mod. Phys.* **1964**, *36*, 844–855.

(39) Langreth, D. C.; Perdew, J. P. The exchange-correlation energy of a metallic surface. *Solid State Communications* **1975**, *17*, 1425–1429.

(40) Gunnarsson, O.; Lundqvist, B. I. Exchange and correlation in atoms, molecules, and solids by the spin-density-functional formalism. *Phys. Rev. B* **1976**, *13*, 4274–4298.

(41) Langreth, D. C.; Perdew, J. P. Exchange-correlation energy of a metallic surface wave-vector analysis. *Phys. Rev. B* **1977**, *15*, 2884.

(42) Andersson, Y.; Langreth, D. C.; Lundqvist, B. I. van der Waals Interactions in Density-Functional Theory. *Phys. Rev. Lett.* **1996**, *76*, 102–105.

(43) Dobson, J. F.; Wang, J. Successful Test of a Seamless van der Waals Density Functional. *Phys. Rev. Lett.* **1999**, *82*, 2123–2126.

(44) Furche, F. Molecular tests of the random phase approximation to the exchange-correlation energy functional. *Phys. Rev. B* **2001**, *64*, 195120.

(45) Perdew, J. P.; Schmidt, K. Jacob's ladder of density functional approximations for the exchange-correlation energy. AIP Conference Proceedings. 2001; pp 1–20.

(46) Harl, J.; Kresse, G. Accurate Bulk Properties from Approximate Many-Body Techniques. *Phys. Rev. Lett.* **2009**, *103*, 056401.

(47) Ren, X.; Rinke, P.; Scheffler, M. Exploring the random phase approximation: Application to CO adsorbed on Cu (111). *Phys. Rev. B* **2009**, *80*, 045402.

(48) Harl, J.; Schimka, L.; Kresse, G. Assessing the quality of the random phase approximation for lattice constants and atomization energies of solids. *Phys. Rev. B* **2010**, *81*, 115126.

(49) Bao, J. L.; Yu, H. S.; Duanmu, K.; Makeev, M. A.; Xu, X.; Truhlar, D. G. Density Functional Theory of the Water Splitting Reaction on Fe(0): Comparison of Local and Nonlocal Correlation Functionals. *ACS Catal.* **2015**, *5*, 2070–2080.

(50) Schimka, L.; Harl, J.; Stroppa, A.; Grüneis, A.; Marsman, M.; Mittendorfer, F.; Kresse, G. Accurate surface and adsorption energies from many-body perturbation theory. *Nat. Mater.* **2010**, *9*, 741–744.

(51) Karlický, F.; Lazar, P.; Dubecky, M.; Otyepka, M. Random phase approximation in surface chemistry: Water splitting on iron. *J. Chem. Theory Comput.* **2013**, *9*, 3670–3676.

(52) Kresse, G.; Hafner, J. Ab initio molecular dynamics for liquid metals. *Phys. Rev. B* **1993**, *47*, 558.

(53) Kresse, G.; Hafner, J. Ab initio molecular-dynamics simulation of the liquid-metal–amorphous-semiconductor transition in germanium. *Phys. Rev. B* **1994**, *49*, 14251.

(54) Kresse, G.; Furthmüller, J. Efficiency of ab-initio total energy calculations for metals and semiconductors using a plane-wave basis set. *Comput. Mater. Sci.* **1996**, *6*, 15–50.

(55) Kresse, G.; Furthmüller, J. Efficient iterative schemes for ab initio total-energy calculations using a plane-wave basis set. *Phys. Rev. B* **1996**, *54*, 11169.

(56) Kresse, G.; Joubert, D. From ultrasoft pseudopotentials to the projector augmented-wave method. *Phys. Rev. B* **1999**, *59*, 1758.

(57) Chen, C.-S.; Lin, J.-H.; Lai, T.-W.; Li, B.-H. Active sites on Cu/SiO2 prepared using the atomic layer epitaxy technique for a low-temperature water–gas shift reaction. *J. Catal.* **2009**, *263*, 155–166.

(58) Prats, H.; Gamallo, P.; Sayós, R.; Illas, F. Unexpectedly large impact of van der Waals interactions on the description of heterogeneously catalyzed reactions: the water gas shift reaction on Cu(321) as a case example. *Physical Chemistry Chemical Physics* **2016**, *18*, 2792–2801.

(59) Monkhorst, H.; Pack, J. Special points for Brillouin-zone integrations. *Phys. Rev. B* **1976**, *13*, 5188.

(60) Svensson, M.; Humbel, S.; Froese, R.; Matsubara, T.; Sieber, S.; Morokuma, K. ONIOM: a multilayered integrated MO + MM method for geometry optimizations and single point energy predictions. A test for Diels-Alder reactions and $Pt(P(t\text{-}Bu)_3)_2 +$ H_2 oxidative addition. *J. Phys. Chem.* **1996**, *100*, 19357–19363.

(61) Harl, J.; Kresse, G. Cohesive energy curves for noble gas solids calculated by adiabatic connection fluctuation-dissipation theory. *Phys. Rev. B* **2008**, *77*, 045136.

(62) Kaltak, M.; Klimeš, J.; Kresse, G. Low scaling algorithms for the random phase approximation: Imaginary time and Laplace transformations. *J. Chem. Theory Comput.* **2014**, *10*, 2498–2507.

(63) Mills, G.; Jónsson, H. Quantum and thermal effects in H_2 dissociative adsorption: Evaluation of free energy barriers in multidimensional quantum systems. *Phys. Rev. Lett.* **1994**, *72*, 1124–1127.

(64) Jónsson, H.; Mills, G.; Jacobsen, K. W. In *Classical and Quantum Dynamics in Condensed Phase Simulations*; Berne, B. J., Ciccotti, G., Coker, D. F., Eds.; 1998.

(65) Henkelman, G.; Uberuaga, B. P.; Jónsson, H. A climbing image nudged elastic band method for finding saddle points and minimum energy paths. *J. Chem. Phys.* **2000**, *113*, 9901–9904.

(66) Henkelman, G.; Jónsson, H. A dimer method for finding saddle points on high dimensional potential surfaces using only first derivatives. *The Journal of Chemical Physics* **1999**, *111*, 7010–7022.

(67) Ochterski, J. W. Thermochemistry in Gaussian. 2000; `https://gaussian.com/thermo/`.

(68) Mcquarrie, D. A.; Simon, J. D. *Molecular Thermodynamics*; University Science Books,U.S., 1999.

(69) Frisch, M. J.; Trucks, G. W.; Schlegel, H. B.; Scuseria, G. E.; Robb, M. A.; Cheeseman, J. R.; Scalmani, G.; Barone, V.; Petersson, G. A.; Nakatsuji, H. et al. Gaussian 09 Revision E.01. Gaussian Inc. Wallingford CT 2009.

(70) Dunning Jr, T. Gaussian basis sets for use in correlated molecular calculations. I. The atoms boron through neon and hydrogen. *J. Chem. Phys.* **1989**, *90*, 1007–1023.

(71) Koryabkina, N.; Phatak, A.; Ruettinger, W.; Farrauto, R.; Ribeiro, F. Determination of kinetic parameters for the water-gas shift reaction on copper catalysts under realistic conditions for fuel cell applications. *J. Catal.* **2003**, *217*, 233–239.

(72) Momma, K.; Izumi, F. VESTA 3for three-dimensional visualization of crystal, volumetric and morphology data. *Journal of Applied Crystallography* **2011**, *44*, 1272–1276.

(73) Rodriguez, J. A.; Clendening, W. D.; Campbell, J. M.; Min, W.; Campbell, C. T. Chemisorption studies on Cs/Cu(110): Model studies of cesium promoters on copper-based catalysts. *J. Vac. Sci. Technol. A.* **1989**, *7*, 2118–2120.

(74) *MATLAB (Version R2019a), The MathWorks Inc., Natick, MA, USA*

(75) Perdew, J. P.; Wang, Y. Accurate and simple analytic representation of the electron-gas correlation energy. *Physical Review B* **1992**, *45*, 13244–13249.

(76) Wellendorff, J.; Lundgaard, K.; Møgelhøj, A.; Petzold, V.; Landis, D.; Nørskov, J.; Bligaard, T.; Jacobsen, K. Density functionals for surface science: Exchange-correlation model development with Bayesian error estimation. *Phys. Rev. B* **2012**, *85*, 235149.

(77) Tao, J.; Perdew, J. P.; Staroverov, V. N.; Scuseria, G. E. Climbing the Density Functional Ladder: Nonempirical Meta–Generalized Gradient Approximation Designed for Molecules and Solids. *Phys. Rev. Lett.* **2003**, *91*, 146401.

(78) Perdew, J. P.; Ruzsinszky, A.; Csonka, G. I.; Constantin, L. A.; Sun, J. Workhorse Semilocal Density Functional for Condensed Matter Physics and Quantum Chemistry. *Phys. Rev. Lett.* **2009**, *103*, 026403.

(79) Perdew, J. P.; Ruzsinszky, A.; Csonka, G. I.; Constantin, L. A.; Sun, J. Erratum:

Workhorse Semilocal Density Functional for Condensed Matter Physics and Quantum Chemistry [Phys. Rev. Lett.103, 026403 (2009)]. *Phys. Rev. Lett.* **2011**, *106*, 179902.

(80) Zhao, Y.; Truhlar, D. G. A new local density functional for main-group thermochemistry, transition metal bonding, thermochemical kinetics, and noncovalent interactions. *J. Chem. Phys* **2006**, *125*, 194101.

(81) Sun, J.; Ruzsinszky, A.; Perdew, J. Strongly Constrained and Appropriately Normed Semilocal Density Functional. *Phys. Rev. Lett.* **2015**, *115*, 036402.

(82) Perdew, J. P.; Ernzerhof, M.; Burke, K. Rationale for mixing exact exchange with density functional approximations. *J. Chem. Phys* **1996**, *105*, 9982–9985.

(83) Adamo, C.; Barone, V. Toward reliable density functional methods without adjustable parameters: The PBE0 model. *The Journal of Chemical Physics* **1999**, *110*, 6158–6170.

(84) Becke, A. D. Density-functional thermochemistry. III. The role of exact exchange. *J. Chem. Phys* **1993**, *98*, 5648–5652.

(85) Valiev, M.; Bylaska, E.; Govind, N.; Kowalski, K.; Straatsma, T.; Dam, H. V.; Wang, D.; Nieplocha, J.; Apra, E.; Windus, T. et al. NWChem: A comprehensive and scalable open-source solution for large scale molecular simulations. *Computer Physics Communications* **2010**, *181*, 1477–1489.

(86) Linstrom, P., Mallard, W., Eds. *NIST Chemistry WebBook, NIST Standard Reference Database Number 69*; National Institute of Standards and Technology, Gaithersburg MD, 20899, retrieved January 16, 2018.

(87) Vollmer, S.; Witte, G.; Wöll, C. *Catalysis Letters* **2001**, *77*, 97–101.

(88) Mariani, C.; Horn, K. Orientation of water adsorbed on Cu(110). *Surface Science* **1983**, *126*, 279–285.

(89) Anger, G.; Winkler, A.; Rendulic, K. Adsorption and desorption kinetics in the systems H2/Cu(111), H2/Cu(110) and H2/Cu(100). *Surface Science* **1989**, *220*, 1–17.

(90) Lackey, D.; Schott, J.; Straehler, B.; Sass, J. K. Water adsorption on clean and caesium covered Cu{110}. *The Journal of Chemical Physics* **1989**, *91*, 1365–1373.

(91) Kojima, I.; Kiyomiya, M.; Yasumori, I. Thermal Desorption of Hydrogen Adsorbed on Copper Surface. *Bulletin of the Chemical Society of Japan* **1980**, *53*, 2123–2127.

(92) Andersson, K.; Gómez, A.; Glover, C.; Nordlund, D.; Öström, H.; Schiros, T.; Takahashi, O.; Ogasawara, H.; Pettersson, L.; Nilsson, A. Molecularly intact and dissociative adsorption of water on clean Cu(110): A comparison with the water/Ru(001) system. *Surface Science* **2005**, *585*, L183–L189.

(93) Tang, Q.-L.; Chen, Z.-X. Density functional slab model studies of water adsorption on flat and stepped Cu surfaces. *Surface Science* **2007**, *601*, 954–964.

(94) Studt, F.; Behrens, M.; Abild-Pedersen, F. Energetics of the Water–Gas-Shift Reaction on the Active Sites of the Industrially Used Cu/ZnO/Al_2O_3 Catalyst. *Catal. Lett.* **2014**, *144*, 1973–1977.

(95) Campbell, C. Finding the rate-determining step in a mechanism: comparing dedonder relations with the Degree of Rate Control. *J. Catal.* **2001**, *204*, 520–524.

(96) Nakamura, J.; Kushida, Y.; Choi, Y.; Uchijima, T.; Fujitani, T. X-ray photoelectron spectroscopy and scanning tunnel microscope studies of formate species synthesized on Cu(111) surfaces. *J. Vac. Sci. Technol. A* **1997**, *15*, 1568–1571.

(97) Nishimura, H.; Yatsu, T.; Fujitani, T.; Uchijima, T.; Nakamura, J. Synthesis and decomposition of formate on a Cu(111) surface - kinetic analysis. *J. Mol. Catal. A: Chem.* **2000**, *155*, 3–11.

(98) Nakamura, I.; Nakano, H.; Fujitani, T.; Uchijima, T.; Nakamura, J. Synthesis and decomposition of formate on Cu(111) and Cu(110) surfaces: Structure sensitivity. *J. Vac. Sci. Technol. A* **1999**, *17*, 1592–1595.

(99) Taylor, P.; Rasmussen, P.; Ovesen, C.; Stoltze, P.; Chorkendorff, I. Formate synthesis on Cu(100). *Surf. Sci.* **1992**, *261*, 191–206.

(100) Yatsu, T.; Nishimura, H.; Fujitani, T.; Nakamura, J. Synthesis and decomposition of formate on a Cu/SiO2 catalyst: Comparison to Cu(111). *J. Catal.* **2000**, *191*, 423–429.

(101) Taylor, P.; Rasmussen, P.; Chorkendorff, I. Formate synthesis on Cu(100). *J. Phys.: Condens. Matter* **1991**, *3*, S59.

(102) Campbell, C. T.; Sellers, J. R. V. The Entropies of Adsorbed Molecules. *Journal of the American Chemical Society* **2012**, *134*, 18109–18115.

(103) Campbell, C. T.; Sprowl, L. H.; Árnadóttir, L. Equilibrium Constants and Rate Constants for Adsorbates: Two-Dimensional (2D) Ideal Gas, 2D Ideal Lattice Gas, and Ideal Hindered Translator Models. *The Journal of Physical Chemistry C* **2016**, *120*, 10283–10297.

(104) Campbell, C. T.; Árnadóttir, L.; Sellers, J. R. V. Kinetic Prefactors of Reactions on Solid Surfaces. *Zeitschrift für Physikalische Chemie* **2013**, *227*.

(105) Grimme, S.; Antony, J.; Ehrlich, S.; Krieg, H. A consistent and accurate ab initio parametrization of density functional dispersion correction (DFT-D) for the 94 elements H-Pu. *The Journal of Chemical Physics* **2010**, *132*, 154104.

(106) Zhao, Z.-J.; Li, Z.; Cui, Y.; Zhu, H.; Schneider, W. F.; Delgass, W. N.; Ribeiro, F.; Greeley, J. Importance of metal-oxide interfaces in heterogeneous catalysis: A combined DFT, microkinetic, and experimental study of water-gas shift on Au/MgO. *Journal of Catalysis* **2017**, *345*, 157–169.

Graphical TOC Entry